



Cyprus
University of
Technology



杭州电子科技大学
HANGZHOU DIANZI UNIVERSITY

Master's thesis

Methods for improving MR thermometry in focused ultrasound

Yu Weng

Limassol, MAY 2025



MSc in Electronics Science
and Technology

CYPRUS UNIVERSITY OF TECHNOLOGY

Faculty of Engineering and Technology

Department of Electrical Engineering, Computer Engineering, and Informatics

Master's thesis

Methods for improving MR thermometry in focused ultrasound

Yu Weng

Supervisor

Christakis Damianou

Limassol, MAY 2025

Approval Form

Master's thesis

Methods for improving MR thermometry in focused ultrasound

Presented by

Yu Weng

Supervisor: Christakis Damianou

Member of the committee: Jufeng Zhao

Member of the committee: Anastasia Antoniou

Cyprus University of Technology
Limassol, MAY 2025

Copyrights

Copyright © 2025 Yu Weng

All rights reserved.

The approval of the dissertation by the Department of Electrical Engineering, Computer Engineering, and Informatics does not necessarily imply the approval by the Department of the views of the writer.

Acknowledgements

I would like to extend my heartfelt gratitude to Professor Christakis Damianou, Professor Zhao Jufeng, and Mr. Nikolas Evripidou. During the research on the “Methods for Improving MR Thermometry in Focused Ultrasound” project, Professor Christakis Damianou not only introduced me to this valuable research direction but also provided meticulous guidance and unwavering support throughout the process.

In the progression of the project, both Professor Christakis Damianou and Professor Zhao Jufeng offered invaluable insights into refining the research methodology, optimizing experimental approaches, and analyzing data, from which I have greatly benefited. In the study of traditional methods for heatmap denoising and temperature smoothing, their unique perspectives and extensive expertise provided significant guidance and reference for my research work.

I am also sincerely grateful to Mr. Nikolas Evripidou, whose insightful discussions on experimental implementation details greatly contributed to the smooth execution of this project.

This study has not only enhanced my theoretical knowledge and experimental skills but also motivated me to strive further in my future academic endeavors.

Once again, I would like to express my sincerest gratitude to Professor Christakis Damianou, Professor Zhao Jufeng, and Mr. Nikolas Evripidou!

ABSTRACT

Magnetic Resonance-guided Focused Ultrasound (MRgFUS) is an advanced medical treatment technology that combines focused ultrasound with MRI imaging. It enables real-time monitoring of temperature changes in the treatment area, assisting physicians in evaluating the effectiveness of tumor ablation and tissue treatment. However, heat map images are often affected by noise and temperature profiles may exhibit fluctuations, which can impair the accurate assessment of treatment outcomes during treatment. To address this issue, this paper proposes a heatmap image denoising method that combines GrabCut with automatically detects and adaptively modifies phase variations algorithm (GB-DMPV) and applies the Hampel–Gaussian algorithm to smooth the temperature profiles. GB-DMPV combines GrabCut segmentation with consistent region analysis and replaces high-variation areas using baseline images for effective denoising. Hampel–Gaussian combines a Hampel filter to detect outliers with a Gaussian trinomial model for temperature profile smoothing. The dataset used in this study was collected using the Siemens Magnetom Vida system. Experimental results demonstrate that the proposed denoising and temperature profile smoothing methods perform effectively under current conditions. These successfully remove noise from heat map images, reduce short-term fluctuations in the temperature profiles and preserve target areas in the images, thereby enhancing the accuracy and reliability of treatment outcome evaluations.

Keywords: MRgFUS, Heat map denoising, Temperature profile smoothing, GrabCut, Hampel filter, Gaussian trinomial model

TABLE OF CONTENTS

ABSTRACT	v
TABLE OF CONTENTS	vi
LIST OF TABLES	viii
LIST OF FIGURES	ix
LIST OF ABBREVIATIONS	xii
1 Introduction	1
1.1 Research background	1
1.1.1 Principle of MRgFUS	1
1.1.2 Development of MRgFUS	2
1.2 Technical challenges and significance	3
1.3 Main contributions	3
1.4 Structure of the paper	4
2 Literature Review	5
2.1 MR thermometry	5
2.1.1 Proton Resonance Frequency Shift Method	5
2.1.2 T1 relaxation time method	6
2.1.3 T2 relaxation time method	7
2.1.4 Proton Density	7
2.1.5 Diffusion-weighted imaging method	7
2.1.6 Magnetization transfer	8
2.1.7 Chemical shift method	9
2.2 Heat map images denoising	9
2.2.1 Denoising based on traditional methods	9
2.2.2 Denoising based on deep learning methods	11
2.3 Smoothing of temperature curves	13
2.3.1 Statistical smoothing methods	13
2.3.2 Fitting smoothing methods	14
2.3.3 Wavelet transform smoothing method	15
2.3.4 Deep learning smoothing methods	16

3 Research Methodology	17
3.1 MR thermometry	17
3.2 GB-DMPV	18
3.2.1 Magnitude image denoising (GB)	20
3.2.2 Phase image denoising (DMPV)	22
3.3 Hampel–Gaussian	27
3.3.1 Gaussian trinomial model	28
3.3.2 Hampel outlier detection	30
3.3.3 Outlier data fixing	31
3.4 Custom methods developed for comparison	32
3.4.1 Heat map denoising	32
3.4.2 Temperature profile smoothing	33
4 Experimental Results	36
4.1 Setting and Description	36
4.2 GB-DMPV	36
4.2.1 Visual Effects	36
4.2.2 Ablation Study	38
4.2.3 The Effect of Denoising on the Temperature Profile	39
4.2.4 Summary	41
4.3 Hampel–Gaussian	41
4.3.1 Comparison of Visual Effects in Experiment	41
4.3.2 Outliers with different data repairing	42
4.3.3 Summary	43
5 Discussion	44
5.1 Effectiveness of GB-DMPV in Heat Map Denoising	44
5.2 Advantages of Hampel-Gaussian in Temperature Profile Smoothing	44
6 Conclusion	45
BIBLIOGRAPHY	46

LIST OF TABLES

LIST OF FIGURES

1.1	Properties of MR temperature images which have to be balanced to achieve an efficient temperature monitoring.	3
3.1	The custom software interface.	18
3.2	The flowchart for noise removal. The left part is magnitude image denoising and the right part is phase image denoising.	19
3.3	The results of consistent region detection marked in red: (a) and (b) represent consistent regions at different times in the magnitude image.	20
3.4	The results of consistent region detection marked in red: (a) and (b) represent consistent regions at different times in the phase image.	23
3.5	The results of target region extraction: (a) consistent region and target region in the magnitude image with the consistent region marked in red and the target region marked in blue. (b) consistent region and target region in the phase image with the consistent region marked in yellow and the target region marked in green.	23
3.6	The flowchart for the baseline process.	24
3.7	The results of baseline: (a) The first three phase images are captured in the off-state. From left to right, they are image1, image2 and image3. (b) Fused image (baseline).	25
3.8	All detected changed regions within the consistent regions are marked in yellow.	27
3.9	The flowchart of the temperature profile smoothing process.	28
3.10	The result of Gaussian trinomial model fitting profile in (a) and (b). The blue one represents original and the red one is fitted profile.	30
3.11	The result of the Hampel outlier detection: (a) use original data to draw a profile. (b) outliers detect in original data.	31
3.12	The results of peak area outlier handling.(a) displays the original data along with the Gaussian trinomial model. (b) highlights the outliers, which are marked with red dots. (c) shows the result after applying the peak area outlier handling method and (d) shows the result without using the method.	32
3.13	The process and the result of custom heat map denoising: (a) the image shows the YOLO model detecting target areas. (b) use HSV to extract noise. (c) the result of heat map denosing.	33
3.14	The process and the result of the first custom profile smoothing: (a) the image shows original temperature data. (b) use the first comparative method to correct. (c) the result of outliers detection.	34
3.15	MATLAB fitted profile aligned with the observed trend.	34

3.16 The process and the result of the second custom profile smoothing: (a) the image shows original temperature data. (b) use the second comparative method to correct. (c) the result of outliers detection.	35
4.1 The results of heat map denoising:(a) Noisy image, (b) Gaussian filter, (c) Bilateral filter, (d) NLM, (e) TV, (f) YOLO-HSV and (g) GB-DMPV.	37
4.2 Visual comparisons of heat map denoising methods in ablation study: (a) Noisy image, (b) Fixed GB, (c) Fixed DMPV, (d) GB-DMPV.	39
4.3 The result of the effect of denoising on the temperature profile. (a) the temperature profile before denoising and (b) the temperature profile after denoising.	40
4.4 The result of temperature profile smoothing. (a) original temperature data, (b) LOESS, (C) the first comparative method which is introduced in subsubsection 3.4.2.1, (d) the second comparative method which is introduced in subsubsection 3.4.2.2 and (e) Hampel-Gaussian.	42
4.5 The result of outliers with different data repairing: (a) Original temperature data, (b) Hampel-Gaussian, (C) Remove outlier segments process and (d) Remove peak region process.	43

LIST OF ABBREVIATIONS

MRgFUS	Magnetic Resonance-guided Focused Ultrasound
MRI	Magnetic Resonance Imaging
HIFU	High-Intensity Focused Ultrasound
BBB	Blood-Brain Barrier
MR	Magnetic Resonance
GB-DMPV	GrabCut with automatically detects and adaptively modifies phase variations
PRFS	Proton Resonance Frequency Shift
PRF	Proton resonance frequency
GRE	Gradient echo
SNR	Signal-to-noise ratio
DWI	Diffusion-Weighted Imaging
MT	Magnetization transfer
RF	Radio frequency
WASSC	Water and fat shift chemical shift
ABF	Adaptive Bilateral Filter
NLM	Non-Local Means
RNLM	Robust Non-Local Means
TV	Total Variation
CNNs	Convolutional Neural Networks
GAN	Generative Adversarial Networks
DnCNN	Denoising Convolutional Neural Network
ResU-Net	Residual U-Net
RDU-Net	Residual Dense U-Net
CycleGAN	Cycle-Consistent Generative Adversarial Network
WGAN	Wasserstein Generative Adversarial Network
DIP	Deep Image Prior
MA	Moving Average
SG filter	Savitzky-Golay filter
LPR	Local polynomial regression
LOESS	Local Weighted Regression
GCV	Generalized Cross-Validation
DWT	Discrete Wavelet Transform
PRFS	Proton Resonance Frequency Shift
GMM	Gaussian Mixture Models
EM	Expectation-Maximization
CEM43	Cumulative equivalent minutes at 43°C
AFP	Automatic Focal Point
DICOM	Digital Imaging and Communications in Medicine
ROI	Region of Interest
PSNR	Peak Signal-to-Noise Ratio
SSIM	Structural Similarity Index Measure
YOLO	You Only Look Once
MAD	median absolute deviation

1 Introduction

1.1 Research background

As the trend of younger onset of diseases intensifies, thermal therapy is gradually emerging as a significant treatment modality for hyperplasia, tumors and malignancies, alongside traditional surgical procedures. Common thermal treatment techniques include radio-frequency ablation, microwave therapy, laser ablation and focused ultrasound. Among these, focused ultrasound has garnered significant attention due to its non-invasive nature and has been successfully applied in various clinical fields[1] [2]. Magnetic Resonance-guided Focused Ultrasound (MRgFUS) is a non-invasive therapeutic technology. It integrates Magnetic Resonance Imaging (MRI) for precise localization with High-Intensity Focused Ultrasound (HIFU) to induce thermal effects, enabling the precise ablation of diseased tissues without the need for surgical incisions. This technology eliminates the inherent invasiveness of traditional surgical procedures while enabling real-time MRI monitoring. This dual capability ensures precise treatment and enhances procedural safety, providing patients with a superior therapeutic alternative.

1.1.1 Principle of MRgFUS

When a voltage difference is applied across the two poles of a piezoelectric material (ceramic materials, mainly lead zirconate titanate), it undergoes deformation. When a sine wave excitation signal, with a frequency exceeding the human hearing range (above 20 kHz), is applied to the piezoelectric material, the material deforms either by stretching or compressing according to this frequency, generating vibrations. These vibrations are then radiated into the surrounding medium and form ultrasonic waves.

Ultrasonic waves are a type of mechanical longitudinal wave. During propagation, they cause variations in the density of the medium's molecules, allowing energy to spread. Mechanical waves attenuate during propagation as a result of scattering and absorption by the medium with the absorbed mechanical energy mostly converted into heat. Soft tissues have a low absorption rate for ultrasound, so the sound field can reach deeper tissues [3]. When ultrasound waves encounter boundaries between tissues of different densities or sound velocities, it will lose energy such as reflection, refraction or diffraction. This loss is especially significant when the impedance difference between the two media is large. Gaseous tissues and bones have significant impedance differences compared with soft tissues, so ultrasound must avoid areas such as the lungs, digestive tract and brain, where gas, bone and soft tissues are mixed.

When the piezoelectric transducer is made in a spherical shape, it can focus the sound energy in one region (near the center of the sphere). In this region, the sound intensity is high, while the other areas experience minimal influence from the sound field. This allows for high-intensity exposure of specific tissues (such as diseased tissues) for thermal therapy. The size of the focal zone is determined by the geometry of the piezoelectric material and the ultrasound frequency [4]. The focal point can be moved to treat the target area. Focused ultrasound therapy can control the focus position using an acoustic lens or a phased array transducer.

The treatment with focused ultrasound is based on the thermal and mechanical effects of ultrasound on biological tissues. The latter is typically manifested through the interaction between ultrasound and

micro-bubbles. Micro-bubbles can be generated from small gas nuclei in tissues or injected artificially into the treatment area. When ultrasound acts on the micro-bubbles, cavitation occurs. During the acoustic wave cycle, the micro-bubbles are compressed in the positive half-cycle and expand in the negative half-cycle. When the sound intensity is high, the strong compression in the positive half-cycle can cause the micro-bubbles to collapse, generating intense shock waves and high-speed jets that cause tissue damage. Cavitation effects can be stable or transient and both processes can be used for ultrasound therapy [5]. Cavitation also improves the thermal effect of ultrasound.

In the tissue, the absorbed sound energy is converted into heat, causing the tissue to heat up. Thermal therapy can be divided into two categories: mild hyperthermia and thermal ablation. The temperature range for mild hyperthermia is typically between 43-45°C, maintained for several minutes. This temperature is used to directly kill tumor cells or to significantly increase their sensitivity to drugs or radiation [6]. The temperature range for thermal ablation is between 50-80°C and it can cause protein denaturation within a few seconds, leading to tissue coagulation necrosis. During treatment, the surrounding healthy tissue outside the lesion is minimally affected, ensuring safety and accuracy. Furthermore, focused ultrasound eliminates the need for surgical incisions, with sound wave energy transmitted entirely through the exterior, significantly reducing the risk of infection and postoperative complications. This provides patients with a safe and effective treatment option. However, in practical scenarios, acoustic and thermal parameters cannot be known with high precision, and tissue conditions are complex. Therefore, the temperature of tissue needs to be monitored to ensure the safety of the treatment process. Additionally, due to the presence of blood perfusion, a single heating process cannot be prolonged for too long and must achieve the required thermal dose within a short time (usually 1-30 seconds) [7]. Thus, monitoring the treatment process is crucial. MRI plays a key role in MRgFUS by providing precise localization of the treatment area and real-time temperature monitoring. This ensures accurate visualization of tissue distribution and dynamic temperature changes, providing reliable guidance to doctors to adjust treatment parameters in real time. This combination ensures the effectiveness and safety of the treatment.

1.1.2 Development of MRgFUS

In the 1960s, Lele clarified the principles of high-intensity ultrasound for therapeutic use and introduced several related parameter concepts[8]. Building on this theory, focused ultrasound was gradually applied to treat a variety of organs and diseases[9] [10]. However, the clinical application of focused ultrasound progressed slowly, mainly due to challenges in preoperative planning, intraoperative monitoring and postoperative evaluation. It was not until the 1990s that the MRgFUS treatment system emerged, providing an effective technological solution to these issues. The first MRgFUS device was manufactured by GE, which used an automated system to control a single-element transducer within the MRI chamber for the treatment[11]. It was proven that the MRgFUS treatment process is feasible and the first clinical treatment was successfully performed—the ablation of breast cancer[1] [12]. With the development of technology, a phased-array transducer compatible with MRI was successfully developed. By adjusting the excitation signal phases of individual transducer elements, the position and size of the focus can be precisely controlled. This innovation significantly expanded the heating area of the transducer at a fixed position, facilitating precise control of the treatment process and shortening the treatment duration. The combination of MRI guidance and phased-array technology greatly enhanced the clinical practicality of

the focused ultrasound system. On this basis, the ExAblate 2000 MRgFUS treatment system, developed by InSightec, was approved by the FDA for the treatment of uterine fibroids. The system integrates the ultrasound transducer with a precision-controlled mechanical device inside the MRI examination bed and is used in conjunction with the GE 1.5T MRI system. After successfully providing a solution for uterine fibroid treatment, this device was expanded to treat additional clinical indications, such as pain relief for bone tumors. Currently, a system for brain treatments, the ExAblate 4000, has also been successfully developed, enabling the treatment of brain tumors, neuroregulation and blood-brain barrier (BBB) opening[13] [14].

1.2 Technical challenges and significance

The rapid advancement of medical imaging technology has facilitated the widespread adoption of MRgFUS as an advanced treatment modality for tumors and tissue ablation. This technique combines focused ultrasound with MRI imaging, enabling real-time monitoring of temperature changes in the treatment area. This capability provides physicians with crucial data to accurately assess the effectiveness of tumor ablation and tissue treatment. However, despite its considerable promise in clinical practice, significant challenges remain, particularly with respect to temperature monitoring. As shown in Figure 1.1, artifacts and noise should be reduced as much as possible in Magnetic Resonance (MR) temperature monitoring. Because the presence of noise can cause fluctuations in the temperature distribution, it may affect the accuracy of treatment evaluation and clinical decision making. As a result, improving image denoising and smoothing temperature profiles have become key factors in enhancing the precision and reliability of MRgFUS treatments.

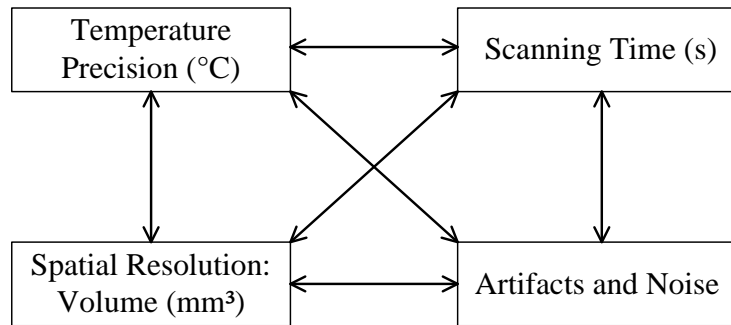


Figure 1.1: Properties of MR temperature images which have to be balanced to achieve an efficient temperature monitoring.

1.3 Main contributions

To overcome the limitations of existing traditional methods and deep learning-based models, this study proposes a method called GB-DMPV, which combines GrabCut with automatically detects and adaptively modifies phase variations. GrabCut is a segmentation-based method that exploits global image information and boundary features to effectively separate target regions from the background, thereby enabling noise removal. Unlike traditional denoising methods, GrabCut minimizes the blurring of critical details, making it especially well-suited for preserving intricate structures in medical images. The innovative phase denoising method DMPV that automatically detects and adaptively modifies phase variations. The

method mainly detects consistent regions and then use baseline to replace identifies changes within those regions. It can remove noise that Grabcut fails to eliminate. Additionally, to enhance the accuracy of temperature evaluation during treatment, this study introduces the Hampel–Gaussian method for temperature profile smoothing. This method combines a Hampel filter for outlier detection with a Gaussian trinomial model to smooth and repair the temperature profile.

1.4 Structure of the paper

The structure of this paper is organized as follows: Chapter 2 provides a comprehensive review of the current research landscape in related fields, including the application and development of MR thermometry, image denoising technologies, and profile smoothing methods. Chapter 3 offers a detailed description of the theoretical foundations and algorithmic implementation of MR thermometry, GB-DMPV, and Hampel–Gaussian. Chapter 4 presents the experimental results, while Chapter 5 offers a discussion to validate the effectiveness of the proposed methods. Finally, Chapter 6 concludes the paper.

2 Literature Review

2.1 MR thermometry

Thermal ablation therapy is currently a very important treatment method for tumors in clinical practice. However, during the process of inactivating tumor tissue, thermal ablation can easily damage surrounding healthy tissues. Since the shape and size of the tumor during thermal treatment are related to the internal thermal distribution of the tissue, real-time temperature monitoring technology can help doctors properly adjust the parameters of the heating equipment [15], while simultaneously observing tissue temperature changes and controlling the heating time points, thereby reducing the side effects of thermal therapy. MRI thermometry is a non-invasive and efficient temperature detection technology. Research has shown that many magnetic resonance parameters are sensitive to temperature. Next, we will explain the specific principles of these temperature measurement methods.

2.1.1 Proton Resonance Frequency Shift Method

In 1966, Hindman first discovered the sensitivity of proton resonance frequency (PRF) to temperature changes, which laid the theoretical foundation for MRI-based temperature measurement techniques[16]. Later, Ishihara and De Pootter, among others, first applied it to magnetic resonance temperature monitoring [17].

The resonance frequency of a nucleus is determined by the magnitude of the local magnetic field it is in. The local field surrounding a nucleus can be expressed as:

$$B_{\text{loc}} = B_0 - B_{\text{os}} = (1 - s)B_0 \quad (2.1)$$

where s is called the shielding constant, and its value depends on the chemical environment of the nucleus. Due to nuclear shielding, the resonance frequency is:

$$\omega = \gamma B_0(1 - s) \quad (2.2)$$

In water molecules, hydrogen nuclei (protons) are shielded by the electrons in the molecule. The shielding of 1H nuclei in free water molecules is more significant than in water molecules with hydrogen bonds. Hydrogen bonds can bind electrons and reduce the shielding effect. When the temperature changes, the structure and number of hydrogen bonds also change. An increase in temperature causes the hydrogen bonds to break, resulting in more water molecules in the hydrogen bond structure, ultimately increasing the shielding effect of electrons, which decreases the local magnetic field B_{loc} and reduces the resonance frequency.

The relationship between the shielding constant and temperature can be described by the following formula:

$$s(T) = \alpha T \quad (2.3)$$

where the temperature range of -15°C to 100°C , the coefficient α is $-1.03 + 0.02 \times 10^{-3}/^{\circ}\text{C}$. This temperature range encompasses the temperature requirements for interventional treatments. With further advancements, PRF-based spectroscopic imaging and phase imaging methods for temperature measurement have emerged.

2.1.1.1 PRF-based spectroscopic imaging

PRF-based spectroscopic imaging primarily measures temperature by comparing the frequency shifts of PRF data in the target region [18]. This method excels in accurately mapping the spatial and temporal distribution of temperature changes, particularly in detecting local temperature variations within specific tissues. However, due to the technical complexity of spectroscopic imaging and the high hardware requirements, its applications are mainly confined to experimental research environments. Further optimizations in real-time performance and operational simplicity are needed to extend its use in broader clinical temperature monitoring scenarios.

2.1.1.2 PRF-based phase imaging

PRF-based phase imaging employs gradient echo (GRE) sequences to quantify temperature changes by measuring phase shifts in the target region. The core principle is that temperature induced PRF shifts result in phase deviations, which are linearly related to temperature changes, as described by the formula[17]:

$$\Delta T = \frac{\phi(T) - \phi(T_0)}{\gamma\alpha B_0 TE} \quad (2.4)$$

where $\phi(T)$ and $\phi(T_0)$ represent the current and reference temperature phase shifts, γ is the gyromagnetic ratio, α is the temperature sensitivity coefficient, B_0 is the main magnetic field strength, and TE is the echo time.

The key advantage of PRF-based phase imaging is that it does not require additional calibration using reference peaks, thereby simplifying the measurement process and enabling efficient detection of temperature changes. However, this technique requires precise imaging sequences and a highly uniform magnetic field environment, making it challenging to implement in complex scenarios.

2.1.2 T1 relaxation time method

The relationship between T1 relaxation time and temperature was first proposed by Bloembergen in 1948 and later applied to MRI thermometry by Park in 1984[19] [20]. However, the sensitivity of T1 relaxation time to temperature changes is not consistent across different tissue types. For instance, T1 relaxation time exhibits low sensitivity to temperature changes in fat-rich tissues but higher sensitivity in water-rich tissues such as muscle or blood. Due to its complexity and dependence on experimental conditions, T1 thermometry still requires further optimization for use in clinical environments.

2.1.3 T2 relaxation time method

In 1987, Nelson and Tung discovered that the T2 relaxation time of aqueous solutions increases with rising temperature[21]. However, the relationship between T2 relaxation time and temperature is influenced by several factors in tissues other than pure water. Studies of ex vivo tissues have shown that the relationship between T2 relaxation time and temperature is nonlinear, limiting the use of T2 thermometry in clinical settings[22].

2.1.4 Proton Density

According to the Boltzmann distribution (Equation 2.5) [23], proton density (PD) is linearly related to the equilibrium magnetization vector M_0 :

$$PD \propto M_0 = \frac{N\gamma^2 h^2 I(I+1)B_0}{3\mu_0 kT} = \chi_0 B_0 \quad (2.5)$$

where N is the number of spins per unit volume, γ is the magnetic ratio, h is Planck's constant, I is the spin quantum number (for atoms, $I = 1/2$), B_0 is the magnetic flux density, μ_0 is the permeability of free space, T is the absolute temperature of the sample, and χ_0 is the magnetic susceptibility.

Since the magnetization M_0 depends on the Boltzmann thermal equilibrium, proton density-weighted images can be used to assess changes in temperature. By calculating the changes in proton density, we can determine the relative temperature. In fact, it is the magnetic susceptibility that changes with temperature, not proton density itself. Magnetic susceptibility reflects the ratio of protons aligned with and against the magnetic field. The change in M_0 is inversely proportional to temperature, and the change in M_0 per unit temperature is approximately $-0.30 \pm 0.01\%$ [24]. This subtle temperature dependence requires images with a very high signal-to-noise ratio (SNR). For instance, a temperature error of 3°C requires an SNR of 100 [25]. To eliminate the influence of T1 relaxation time changes on proton density-based temperature measurements, a relatively long echo time (around 10 seconds) is typically required during scanning.

2.1.5 Diffusion-weighted imaging method

The temperature-dependent diffusion coefficient (D) in Diffusion-weighted imaging method (DWI) describes the Brownian motion of all molecules in a medium. The relationship between temperature and diffusion coefficient is given by [26]:

$$D \approx e^{-\frac{E_a(D)}{kT}} \quad (2.6)$$

Where $E_a(D)$ is the activation energy for the diffusion of water molecules, k is the Boltzmann constant, and T is the absolute temperature. The temperature dependence can be expressed as:

$$\frac{dD}{DdT} = \frac{E_a(D)}{2kT} \quad (2.7)$$

The temperature sensitivity is approximately $2\%/\text{ }^\circ\text{C}$.

The random Brownian motion of molecules causes a random distribution of displacements. In a strong magnetic field gradient, the diffusion of water molecules in tissues leads to the phase dispersion of the signal, with signal attenuation proportional to the distribution of water molecules along the diffusion gradient direction. In the case where the temperature T is unknown and the reference temperature T_{ref} is known, and the diffusion coefficients D and D_{ref} are obtained, the temperature change is expressed as:

$$\Delta T = T - T_{\text{ref}} = \frac{kT_{\text{ref}}^2}{E_a(D)} \left(\frac{D - D_{\text{ref}}}{D_{\text{ref}}} \right) \quad (2.8)$$

where k is a constant and $E_a(D)$ is the function related to the diffusion coefficient.

Assuming the temperature change is small ($\Delta T \ll T_{\text{ref}}$), the activation energy E can be considered temperature-independent. The water molecule diffusion method has been widely applied for non-invasive temperature measurement *in vivo*. This method offers high temperature sensitivity but requires longer acquisition times and is susceptible to motion artifacts. Using echo-planar imaging and line scan techniques can shorten scan times and reduce sensitivity to motion. Another issue is that the relationship between diffusion coefficient and temperature can change non-linearly when tissue conditions change *in vivo*. This is because the diffusion of water molecules in tissues is hindered by various factors, such as cell structure, proteins, and cell membranes. Protein coagulation due to heating can cause significant changes in the diffusion coefficient. Furthermore, non-lethal physiological effects, such as cerebral ischemia, can also alter the diffusion coefficient.

In anisotropic tissues (such as muscle fibers), the movement of water protons depends on the direction of diffusion. To precisely measure temperature, calculating the complete diffusion tensor is often necessary. However, these methods tend to increase scan time compared to single-direction diffusion coefficient measurements. Since diffusion coefficient changes in fat differ from those in water, fat suppression is also required. The phase dispersion effect caused by temperature gradients is much greater than in the T1 method, as the diffusion coefficient method requires longer echo times. Therefore, using spin-echo imaging is more suitable.

2.1.6 Magnetization transfer

Magnetization transfer (MT) techniques use selective radio frequency (RF) pulses in a specific spectral range to target particular water molecules or macromolecules[27]. The temperature-dependent magnetization transfer effect indirectly reflects tissue temperature through changes in MRI signals. The MT effect modifies the relaxation properties of protons in response to RF pulses, enabling indirect temperature measurement.

Although MT techniques can theoretically provide highly sensitive temperature measurements, their accuracy is highly dependent on tissue-specific characteristics. This poses challenges in practical applications, especially in tissues with complex structures or high heterogeneity, where nonlinear signal responses may affect temperature estimation. Consequently, MT thermometry is primarily used in basic research or non-clinical thermal therapies.

2.1.7 Chemical shift method

The chemical shift method is based on the differences in resonance frequencies caused by the magnetic shielding effects of nuclei in different chemical environments. In water and fat molecules, hydrogen nuclei experience distinct chemical environments, leading to a significant chemical shift. MRI can simultaneously detect resonance signals from water and fat peaks and the relative position changes between them can be used to infer temperature variations. The Water and fat shift chemical shift (WASSC) is linearly correlated with temperature changes, allowing for precise temperature measurement through chemical shift monitoring:

$$\Delta\nu = \nu_{\text{water}} - \nu_{\text{fat}} \quad (2.9)$$

where $\Delta\nu$ represents the chemical shift difference, while ν_{water} and ν_{fat} denote the resonance frequencies of water and fat peaks, respectively. Temperature variations can be calculated using the linear regression relationship of the chemical shift difference:

This method is highly sensitive to temperature changes and provides accurate temperature estimates without requiring external calibration. However, it depends on the water-to-fat ratio, requiring a measurable proportion of both components in the region of interest. Low or absent fat content may limit its application. Furthermore, it is sensitive to magnetic field homogeneity, and signal interference from complex or uneven tissue structures may affect its accuracy in temperature measurement.

2.2 Heat map images denoising

2.2.1 Denoising based on traditional methods

Traditional denoising methods can be broadly classified into three main categories: filtering methods, regularization methods, and statistical modeling-based methods. Among these, filtering methods are further divided into those that operate in the spatial domain and those that operate in the transform domain.

2.2.1.1 Denoising based on filtering

The core principle behind spatial domain-based filtering methods is the reduction of noise by smoothing local pixels within the spatial domain of the image. This typically involves calculating the mean or median value of pixels within a local region of the image to eliminate noise. Gaussian filter aims to reduce high-frequency noise in an image by applying a Gaussian kernel, which performs smoothing operations[28]. However, it is important to note that while Gaussian filter effectively removes noise, it also causes blurring of the image details [29]. To address this issue, bilateral filter was developed as a method to preserve edge information by considering both spatial distance and greyscale differences between neighboring pixels [30]. Compared with Gaussian filter, bilateral filter proves to be more effective in denoising, as it preserves edge details better. However, this method comes at a higher computational cost, and the processing speed is relatively slow [31]. In addition, Adaptive Bilateral Filter(ABF) is an emerging denoising method that enhances image clarity by increasing edge slopes while simultaneously reducing noise. Research has demonstrated that ABF can enhance image edges and texture while ef-

fectively denoising, showing superior performance compared to traditional filter methods[32]. Another notable method is Non-Local Means (NLM), which removes noise by performing weighted averaging of similar blocks within the image [33]. In 2014, Zhang et al. proposed an improvement to NLM, the Robust Non-Local Means (RNLM) method, which combines block and pixel filtering strategies to further enhance denoising performance[34].

The fundamental concept of transform domain filter involves transforming the image from the spatial domain to a transform domain (such as the frequency domain or multiscale domain). By leveraging the distinct distribution characteristics of noise and image signals in the transform domain, this approach enables more effective separation and suppression of noise. Song et al. (2014) proposed the wavelet shrinkage method which is an effective technique for removing gaussian noise. However, when dealing with stronger noise levels, it may still lead to a loss of texture information[35]. In response to these limitations, Anandan P et al. proposed a medical image denoising method that combines the fast discrete curvelet transform with an adaptive thresholding algorithm. This approach begins by decomposing the image into curvelet coefficients using the fast discrete curvelet transform. Then noise is removed through the adaptive thresholding algorithm, which helps preserve important image features. Finally, the image is reconstructed using the inverse curvelet transform achieving the desired denoising effect[36].

2.2.1.2 Denoising based on regularization

MRI regularization denoising methods have been shown to be highly effective in preserving image details while suppressing noise. Rudin, Osher, and Fatemi (1992) proposed Total Variation (TV) regularization[37]. Its main idea is to achieve denoising by minimizing the total variation of the image. However, the standard TV model tends to introduce block artifacts in smooth regions (such as uniform areas within tissues), resulting in the appearance of artifacts in these regions. Moreover, TV denoising tends to lose details when high noise levels are present. To address these limitations, several improvements to TV regularization have been proposed. For example, Chambolle proposed a rapid projection algorithm that significantly accelerates the optimization process of TV regularization [38]. Furthermore, higher-order TV regularization models (such as second-order and third-order TV) incorporate higher-order derivatives, which help mitigate the blocking effects and improve the visual quality of smooth regions [39]. Another approach to regularization denoising is sparse representation. This technique is based on the theory of sparsity, which suggests that an image can be sparsely represented in a particular domain (such as wavelet, curvelet, or dictionary representations). The goal is to denoise the image by constraining the sparse coefficients. Elad et al. Proposed the K-SVD algorithm[40] which is a typical implementation of sparse representation, where features are extracted from image data through dictionary learning. This method has been shown to outperform traditional filter techniques, particularly in handling complex textures and structures. However, while sparse representation techniques have demonstrated superior denoising effects, they are computationally more intensive and may require significant resources for large-scale image processing.

2.2.1.3 Denoising based on statistical model

Statistical modeling methods [41] [42] are fundamentally designed to separate noise and signal by leveraging the statistical properties of images and noise through the construction of probabilistic models.

However, these methods often suffer from high computational complexity, strong dependency on noise models, and poor adaptability to real-world complex scenarios.

2.2.2 Denoising based on deep learning methods

With the rapid development of deep learning technology, deep learning methods have gradually become a hotspot in MRI denoising research. An increasing number of deep learning architectures, such as CNN [43], Generative Adversarial Networks (GAN) [44], and DIP, have been proposed for image denoising.

2.2.2.1 Convolutional neural networks

Convolutional Neural Network is a commonly used deep learning model with strong image feature extraction capabilities. CNN can extract local features from images through convolutional layers and reduce the dimensionality of feature maps through pooling layers while preserving important features. Classical CNN denoising models include DnCNN, U-Net, and others.

(1) DnCNN

In 2017, Kai Zhang initially proposed DnCNN, a deep convolutional neural network designed for image denoising. A residual learning strategy is employed to implicitly remove noise by predicting the residual image (noise), thus circumventing the explicit learning of the image a prior model [45]. Subsequently, Wenjing Wang endorsed the DnCNN model and proposed an enhanced convolutional neural network image denoising model DnCNN2 in 2021. This was done with the objective of addressing the shortcomings of conventional denoising techniques and the prolonged convergence time of the algorithm. The proposed model incorporates a channel attention mechanism in the penultimate layer, based on the DnCNN model, which enhances the signal-to-noise ratio and optimizes the noise reduction effect. The algorithm achieves a shorter convergence time compared with traditional deep learning image denoising algorithms. Additionally, it demonstrates improved noise reduction performance and operational efficiency offering significant advantages[46].

(2) U-Net

The U-Net [47] is another CNN structure that is somewhat similar to a self-encoder. It passes information from the encoder to the decoder through jump connections, which better preserve image details. In MRI image denoising, U-Net has the capacity to remove noise while maintaining high resolution. Through intensive research, ResU-Net employs a Residual Block in place of the standard convolutional block in U-Net, thereby accelerating convergence and enhancing feature transfer in deep networks. Gurrola-Ramos J proposed an image denoising method based on a deep residual dense network called RDUNet. This method leverages densely connected convolutional layers to repurpose feature maps and circumvent the gradient vanishing issue, while accelerating the learning process through local residual learning and global residual learning [48]. Subsequent research by Zhang H. led to the proposal of RatUNet, an attention mechanism-based residual U-Net framework for image denoising. The proposed approach enhances the U-Net architecture by integrating residual blocks to increase network depth, refining the downsampling and upsampling processes, and optimizing skip connections. Additionally, It employs depth-separable convolutions and polarized self-attention mechanisms to effectively capture and process

edge information in images. This results cause an enhanced denoising effect and SSIM metrics, as evidenced in the experimental results[49].

2.2.2.2 Generative adversarial network

GAN is a generative model comprising a generator and a discriminator. Through adversarial training of the two, the generator is continuously improved to generate more realistic, clean images. GAN has demonstrated strong generative ability and excellent denoising effect in MRI image denoising. Notable examples of classical GAN denoising models include Cycle-Consistent Generative Adversarial Network (CycleGAN) and Wasserstein Generative Adversarial Network (WGAN).

(1) CycleGAN

CycleGAN is an unpaired GAN structure that achieves mapping from noisy images to noise-free images through cycle-consistency loss, and still achieves a satisfactory denoising effect in the absence of paired data[50].

(2) WGAN

In 2017, Arjovsky and Bottou [51] pointed out that training GAN is challenging because when the discriminator D is fixed, Equation 2.10 may lead to vanishing gradients for the generator.

$$\min_G \max_D L(D, G) = \mathbb{E}_{y \sim p_r} [\log D(y)] + \mathbb{E}_{x \sim p_z} [\log(1 - D(G(x)))] \quad (2.10)$$

In order to solve this problem, two authors proposed an enhanced variant of GAN, called Wasserstein GAN in the same year [52]. The benefit of WGAN in image denoising is Wasserstein distance (also known as the Earth mover's distance), which is capable of providing effective gradients when the generator output does not align with the real image distribution. Nevertheless, it still provides an effective gradient. The feedback to the generator is more gradual than in traditional GAN, resulting in an image that is closer to a noise-free image. Furthermore, Gulrajani et al. proposed an enhanced version of WGANW called Gradient Penalty, which circumvents the limitations of weight clipping through the incorporation of a gradient-paradigm penalty term into the discriminator loss function, thereby guaranteeing the Lipschitz constraint [53][54].

2.2.2.3 Deep image prior

The DIP method enables image recovery by training neural networks to represent image prior information eliminating the need for data labeling. However, the training process is relatively slow, requires significant computational resources, and demonstrates limited generalization ability when handling diverse types of noise or real-world applications.

2.3 Smoothing of temperature curves

2.3.1 Statistical smoothing methods

2.3.1.1 Moving average smoothing filter

The moving average (MA) method is one of the most fundamental and intuitive techniques for smoothing data curves. It involves calculating the average of data points within a sliding window to smooth curve. Hyndman (2011) provides a detailed exploration of the underlying principles of the moving average method[55]. This method offers flexibility in controlling the degree of smoothing by adjusting the window size. Shorter windows are more sensitive to fluctuations, while longer windows are more effective at capturing long-term trends and cyclical changes.

Despite its simplicity, the moving average method has certain limitations. One notable issue is that it assigns equal weight to all data points within the window, which may result in inadequate smoothing when there are abrupt changes in the signal. Additionally, the method is prone to boundary effects, where the smoothing process yields significant deviations at the beginning and end of the series due to insufficient data points available for averaging. This boundary effect can lead to inaccuracies at the edges of the series, ultimately compromising the overall reliability of the smoothed curve.

2.3.1.2 Savitzky-Golay Filter

The Savitzky-Golay filter (SG filter) is a smoothing method based on polynomial fitting, first introduced by Savitzky and Golay in 1964 [56]. This method uses weighted least squares fitting of a polynomial within a sliding window, replacing the original data points with the results of the polynomial fit. The formula can be expressed as:

$$y_i = \sum_{j=-k}^k c_j \cdot x_{i+j} \quad (2.11)$$

Where y_i is the smoothed data point, x_{i+j} is the original data point, c_j is the polynomial regression coefficient, and k is the window size.

Compared with the moving average filter, the Savitzky-Golay filter effectively preserves high-frequency components of the data and can better maintain the details of the original signal. However, this method is more sensitive to abrupt changes and fluctuations, and its performance depends on the appropriate selection of window size and polynomial degree. A window that is too large may lead to over-smoothing of the signal, while a window that is too small may fail to remove noise effectively.

2.3.1.3 Hampel Filter

The Hampel filter is a denoising method based on the median and the absolute deviation, proposed by Hampel et al. [57]. The Hampel filter calculates the median and the absolute deviation of data points within a sliding window. If the deviation of a data point from the median exceeds a certain threshold, the data point is considered an outlier and is replaced by the median of the window.

The mathematical formula for the Hampel filter is typically:

$$x'_i = \begin{cases} x_i & \text{if } |x_i - \text{median}(window)| \leq k \cdot \text{MAD} \\ \text{median}(window) & \text{if } |x_i - \text{median}(window)| > k \cdot \text{MAD} \end{cases} \quad (2.12)$$

Where x_i is the original data point, x'_i is the corrected data point, $\text{median}(window)$ is the median of the window, MAD is the median absolute deviation, and k is the threshold coefficient.

The Hampel filter has strong robustness against outliers, effectively removing abrupt changes and fluctuations while preserving the main features of the data. Compared with traditional moving average filters, the Hampel filter performs better when dealing with data containing extreme noise. However, the Hampel filter typically requires proper selection of window size and threshold. A window that is too small may affect the filtering effect, while a window that is too large may lead to over-smoothing of the signal.

2.3.2 Fitting smoothing methods

Fitting smoothing methods are primarily concerned with the process of data smoothing, whereby a mathematical model is constructed in order to fit the data. Such methods typically include local polynomial regression, local weighted regression, spline interpolation and B-splines.

2.3.2.1 Local polynomial regression

Local polynomial regression(LPR) is a common fitting method initially proposed by Fan and Gijbels (1996) [58]. The method operates by fitting a low-order polynomial (linear or quadratic) within the vicinity of each data point. Subsequently selecting a window of neighboring data points and fitting them using weighted least squares. This approach enables more accurate capture of the local structure and trends of the data. LPR is more effective than simple moving average methods in addressing boundary effects. Avery (2013) provides further insight into the key parameter choices in the LPR method, including the weighting function, neighborhood size and polynomial fitting order. In particular, the study emphasizes the influence of bandwidth (neighborhood size) selection on the degree of smoothing, whereby an appropriate bandwidth is essential to achieve an optimal balance between data smoothing and local detail preservation. An excessively large bandwidth may result in over-smoothing, which suppresses local variations in the data. Conversely, an insufficiently large bandwidth may fail to effectively remove abrupt changes in the curves, leading to insignificant smoothing effects[59].

2.3.2.2 Local weighted regression

The LOESS method fits the surrounding neighborhood of each data point through a locally weighted regression model, employing weighted least squares to estimate the smoothed value for each point [60]. The method is effective in capturing the local structure of the data and is not susceptible to global trends. Moreover, LOESS is capable of handling non-linear relationships and can flexibly adjust the fitting model. The method assigns greater weight to the data points in closer proximity to the current point through the application of a weighting function, thereby facilitating the more accurate capture of the local trend and details. Furthermore, LOESS is capable of effectively reducing the boundary effect through the utilization of local weight.

2.3.2.3 Spline interpolation

Spline interpolation [61] is a technique that employs low-degree polynomials, typically cubic polynomials, to fit data within individual segments. Among these methods, cubic spline interpolation is particularly popular due to its ability to produce smooth curves at data points while maintaining continuity in both the first and second derivatives. However, when data points are sparsely distributed or contain outliers, this approach can lead to oscillations or unnatural curve shapes. Furthermore, in scenarios with significant data variability, it may be prone to overfitting. Bertolazzi et al.(2020) proposed an algorithm for smoothing noisy data using cubic spline curves. The algorithm begins by clustering data points into overlapping groups, with each group approximated by a single cubic curve. Then, weighted least squares combined with a Tikhonov regularization term is applied to fit a cubic curve for each cluster, controlling the smoothness and curvature of the resulting curves. Finally, the overlapping cubic curves are merged through weighted averaging, and spline interpolation is applied to the reconstructed smooth points to construct the final curve [62]. Azizan et al. (2018) investigated two cubic spline interpolation methods for curve smoothing: natural splines and “non-knot” splines. Their study found that “non-knot” splines outperformed natural splines in terms of accuracy for interpolating missing data and produced visually superior results [63].

2.3.2.4 B-splines

B-splines [64] are a widely used smoothing method. The core principle is to represent a curve using a set of basis functions, each associated with a control point in the dataset. This approach provides flexible control over the shape of the curve without the reliance on global constraints typical of traditional polynomial interpolation. Compared to high-degree polynomial interpolation methods, such as Lagrange interpolation, B-splines effectively mitigate oscillations caused by high-degree polynomials. However, selecting appropriate knots is crucial, as poorly chosen knots can significantly affect the curve’s shape and fitting accuracy. Amir W. A. F. W. et al. (2024) proposed a data smoothing method based on Beta Splines. Beta Splines are flexible curves with two shape parameters, enabling more accurate capture of intricate details in complex datasets and better adaptability to outliers. The study integrates the roughness penalty method and Generalized Cross-Validation (GCV) into the Beta Spline smoothing process to identify the optimal fitting curve and refine the shape parameters. By analyzing the GCV colormap, the best curve can be determined. This approach offers greater flexibility compared to traditional methods, effectively handling various types of time series data and improving the accuracy [65].

2.3.3 Wavelet transform smoothing method

Wavelet transform is a multi-scale analysis technique that enables decomposition across various scales to extract low-frequency components while effectively removing high-frequency noise. Mallat (1989) proposed the Discrete Wavelet Transform (DWT) [66], which decomposes a signal into multiple sub-signals corresponding to different frequency bands. By analyzing the characteristics of each frequency band, DWT can selectively remove abrupt changes while preserving the main structure of the signal. This method offers excellent time-frequency localization properties, allowing feature extraction at multiple scales [67]. Compared to traditional smoothing methods, wavelet transform more precisely retains critical details within the signal while eliminating high-frequency components. However, wavelet transform also

has limitations, particularly in selecting appropriate wavelet basis functions and scales, which require meticulous tuning. Different wavelet basis functions exhibit varying levels of adaptability to signals, and improper selection may lead to ineffective feature extraction or even information loss.

Dai X. et al. (2019) proposed a novel method based on DWT to remove abrupt changes in data. The core concept of this method is to preserve coefficients essential for reconstructing the signal while setting all other coefficients to zero. Numerical simulations revealed that the first eight detail coefficients at each decomposition level are crucial for signal reconstruction. Additionally, curve fitting techniques and correlation analysis were introduced as supplementary measures based on the dataset's characteristics to further enhance the effectiveness of removing abrupt changes [68].

2.3.4 Deep learning smoothing methods

With the rapid advancement of deep learning, data smoothing methods based on deep learning have increasingly attracted attention of researchers. By training a model to learn the underlying patterns in data, deep learning approaches can achieve more flexible and accurate smoothing. For instance, CNN have demonstrated significant success in smoothing applications. These methods excel in automatically learning the nonlinear relationships within data, eliminating the need for manually predefined smoothing rules. Particularly when dealing with complex nonlinear data, deep learning methods can better reveal the intrinsic structure of the dataset. However, these methods typically require large amounts of training data, and the model training process is complex with high computational costs.

3 Research Methodology

3.1 MR thermometry

In this study, the Proton Resonance Frequency Shift (PRFS) method is employed. The PRFS method utilizes the sensitivity of Proton Resonance Frequency (PRF) to temperature, enabling real-time, non-invasive and precise temperature measurements. This is particularly beneficial in treatments such as tumor thermal ablation, where it assists physicians in monitoring temperature changes during the procedure, thereby ensuring the safety and efficacy of the treatment.

Our team develops a software for processing and analyzing thermal imaging data during MRgFUS treatments. First, the software loads the MRI magnitude and phase images and the GB-DMPV method proposed in this paper is applied to optimize the images to reduce noise interference. Next, the temperature distribution of the target area is calculated based on phase changes (using the PRF principle in MRI) and a heat map is generated to monitor real-time temperature changes in the treatment area. Based on these temperature data, the thermal dose is calculated. Typically, cumulative equivalent minutes at 43°C (CEM43) is used as a standard to assess whether sufficient heat has been delivered for tissue ablation during the treatment process. The formula used is as follows:

$$\text{CEM43} = \sum \left(\frac{t}{\exp \frac{(T-43)}{\alpha}} \right) \quad (3.1)$$

where t is the duration (in minutes). T is the temperature at each time point (in °C). α is the thermal sensitivity coefficient of the tissue, typically ranging from 0.5 to 1.

In addition, the software tracks the changes in the acoustic focal point (AFP) location to monitor real-time dynamic changes in the treatment area. This ensures that the energy of the focused ultrasound is accurately delivered to the target area, thereby maximizing the treatment effect and avoiding damage to surrounding healthy tissues. The temperature data of the treatment area is also compared with known tissue necrosis thresholds to determine which regions have reached sufficient temperatures for effective tissue ablation. To assist clinicians in real-time monitoring of dynamic changes during the treatment process, the software generates animations that display the spatial distribution of temperature changes and thermal dose during the treatment.

At the same time, the instantaneous temperature changes of each pixel are calculated through the MRI phase images to generate a heat map. The highest temperature value within the rectangular region is extracted, and the time is retrieved from the DICOM image metadata, which is then stored in an Excel file. The Hampel-Gaussian method proposed in this paper is used to detect and repair outliers and fluctuations in the temperature data.

In terms of temperature mapping, the calculated temperature values were color-coded to generate heat maps. This approach visually displays the temperature distribution within the tissue, typically using blue to indicate low-temperature regions and red for high-temperature areas. Heat maps not only reflect the temperature distribution in real-time during the treatment process but also assist physicians in evaluat-

ing the effectiveness and safety of thermal ablation therapy, preventing overheating or overcooling. To better observe the trend of temperature changes over time, a time series of heat maps was generated at 2.4s intervals. This allows physicians to monitor temperature changes in real-time during the treatment, promptly adjust treatment parameters, and ensure the precision and safety of the therapy[69] [70].

The software interface is shown in Figure 3.1. As shown in Figure 3.1, in parameter settings of the software, users can input the "Time on" and "Time off" values, which can be adjusted based on the experimental scenario to set the on and off times. Additionally, users can configure other parameters related to the temperature data processing algorithm, such as the "Alpha" value and "T Tolerance" for temperature tolerance, which help refine the temperature data repair and calibration. Furthermore, users can specify the number of reference points with the "Number Of Reference" setting. Additionally, the "Sonication Area Margin X" and "Y" parameters can be adjusted to modify the margins of the sonication area.

In terms of image loading and processing, the interface provides two main functional buttons: one for loading the Magnitude Digital Imaging and Communications in Medicine (DICOM) images and another for loading the Phase DICOM images. By loading these images, further image analysis can begin. Additionally, the interface offers an option to load the Region of Interest (ROI).

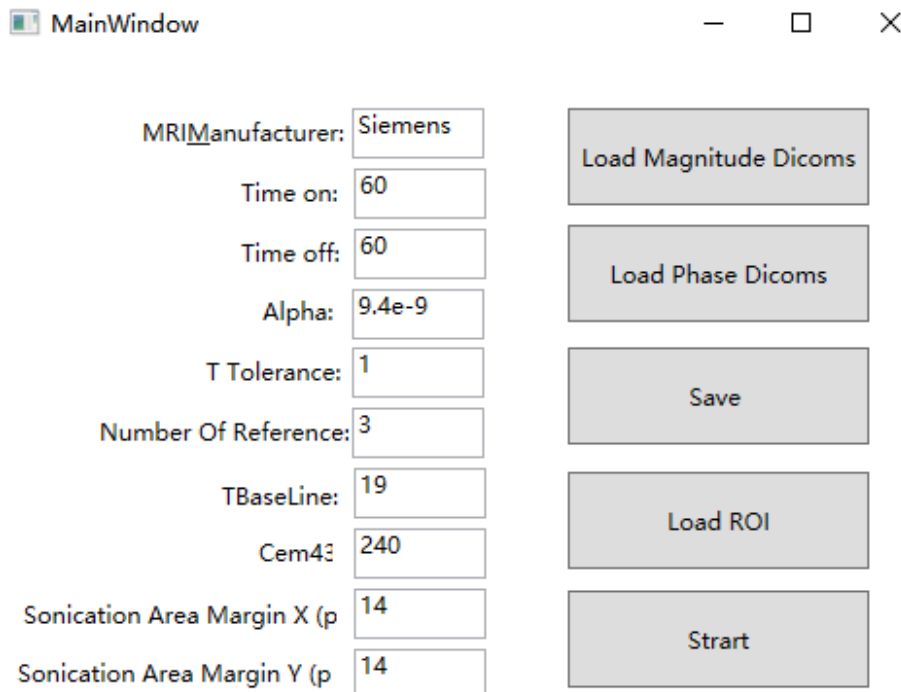


Figure 3.1: The custom software interface.

3.2 GB-DMPV

Due to the unique characteristics of noise in the dataset, we propose a denoising algorithm GB-DMPV that combines the GrabCut with automatically detects and adaptively modifies phase variations in the image. The flowchart illustrating the noise removal process which consists of magnitude image denoising (GB) and phase image denoising (DMPV), is shown in Figure 3.2.

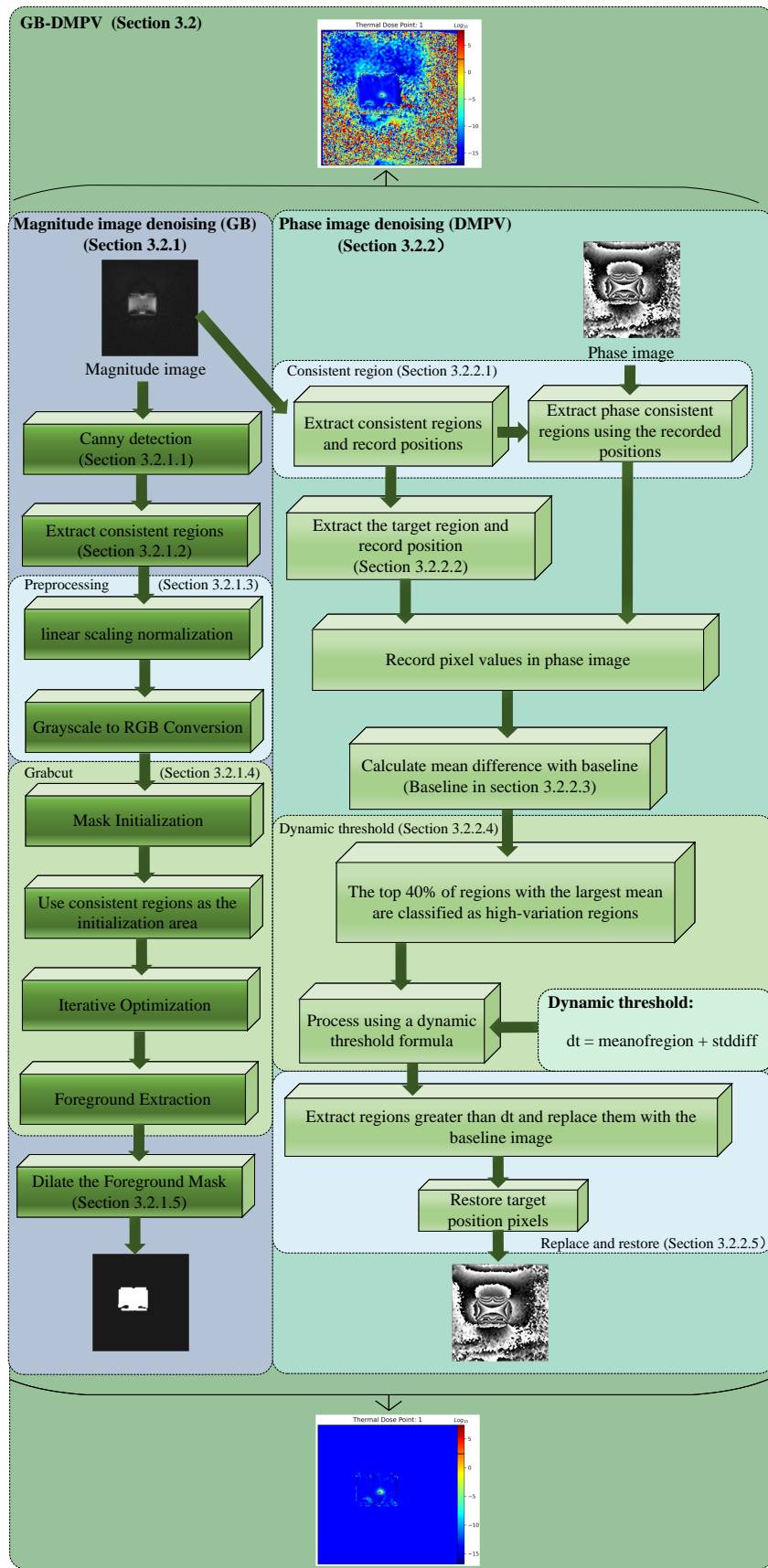


Figure 3.2: The flowchart for noise removal. The left part is magnitude image denoising and the right part is phase image denoising.

3.2.1 Magnitude image denoising (GB)

As shown in Figure 3.2, the magnitude image denoising begins by extracting consistent regions (Figure 3.3) to identify stable areas across multiple images. These regions are then used for linear scaling normalization and converted from grayscale to RGB for GrabCut-based foreground segmentation. The segmentation process includes mask initialization, using the consistent regions as the initialization area, iterative optimization and foreground extraction. After segmentation, the extracted foreground is mapped to unit 16-bit format, and the mask is dilated to refine the region of interest. The final denoised magnitude image serves as a cleaner version of the original image, reducing background noise.

3.2.1.1 Canny detection

Canny edge detection is a classical edge detection algorithm that identifies edges in an image through multiple stages in order to assist in extracting coherent regions. First, the algorithm applies Gaussian filter to the image to remove noise. Then, it calculates the gradient of the image to detect areas with significant intensity changes (with thresholds set at 40 and 160 for edge detection). Next, non-maximum suppression is performed to precisely locate the edge pixels, followed by double thresholding to determine which edges are considered valid. Finally, the algorithm connects edge pixels to generate the final edge map of the image.

3.2.1.2 Consistent regions

In magnitude image denoising, Canny edge detection is applied to each magnitude image to extract contours and calculate the minimum bounding rectangle as the bounding box. Then, the frequency of occurrence of all bounding boxes is counted and the most frequent bounding box is selected as the representative. This indicates the corresponding region is consistent across different images. By removing duplicates, the most stable region is identified as the consistent region. As shown in Figure 3.3 (a) and (b) represent consistent regions at different times in the magnitude image. The red box highlights the ROI in both images.

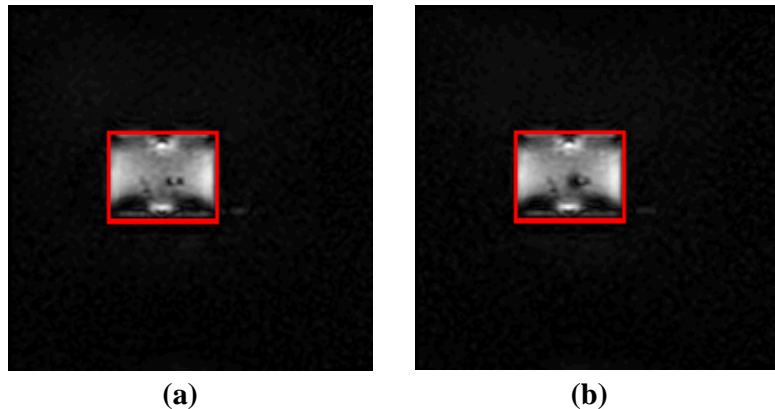


Figure 3.3: The results of consistent region detection marked in red: (a) and (b) represent consistent regions at different times in the magnitude image.

3.2.1.3 Preprocessing

In order to make the image suitable for GrabCut processing, linear scaling normalization is used to normalize the image from the uint16 type to the range of [0, 255]. This method automatically calculates the minimum and maximum values of the image and scales the pixel values proportionally to the specified range. After normalization, the image is converted to the uint8 type, allowing each pixel value to conform to the standard 8-bit image format, making it easier for image processing.

Since GrabCut expects a three-channel color image as input, but the experimental data is a single-channel grayscale image, it also needs to be converted to a three-channel format.

3.2.1.4 GrabCut

(1) Introduction to the GrabCut

The GrabCut algorithm [71] is a graph-based image segmentation method that transforms the image segmentation problem into a minimum cut problem in graph theory, enabling efficient and precise foreground extraction. Specifically, the image is represented as a graph, where each pixel corresponds to a node, and the edges represent the similarity or proximity between pixels. By defining a source node (foreground) and a sink node (background), as well as assigning weights to the edges, the algorithm seeks the minimum cut of the graph to separate it into foreground and background regions.

To evaluate and optimize segmentation quality, GrabCut defines an energy function consisting of two components: the data term and the smoothness term. The data term typically uses features such as the color model to estimate the probability of each pixel belonging to the foreground or background. In contrast, the smoothness term promotes similar labels among adjacent pixels, ensuring smooth and natural segmentation boundaries. Minimizing this energy function allows GrabCut to accurately separate foreground objects from complex backgrounds, achieving effective noise removal.

In practical operation, GrabCut begins by constructing color models for the foreground and background, often using Gaussian Mixture Models (GMM) to describe their color distributions. An initial rectangular region is used to mark parts of the pixels as foreground or background, initializing the GMM and estimating its parameters. The algorithm then uses the Expectation-Maximization (EM) procedure. In the Expectation Step, the GMM is used to compute the probability of each pixel belonging to the foreground or background. In the Maximization step, these probabilities are used to re-estimate the GMM parameters. Once these steps are complete, the Boykov-Kolmogorov algorithm [72] is utilized to efficiently solve the minimum cut problem, yielding the optimal segmentation of foreground and background. This process is iteratively optimized, refining the segmentation results until the energy function converges or the maximum number of iterations is reached.

(2) GrabCut Implementation details

The GrabCut is illustrated in Figure 3.2. Following the preprocessing steps, which include scaling the 16-bit DICOM image to 8-bit and converting it to a three-channel blue, green and red (BGR) format, the GrabCut algorithm is applied for foreground segmentation. After initializing the required parameters, the segmentation process is executed to remove noise from non-consistent regions. Through multiple iterative optimizations, the segmentation result is progressively refined, enhancing both accuracy and detail preservation. Once completed, the GrabCut algorithm outputs a mask labeling each pixel as foreground,

background, or probable foreground/background. By filtering these labels, background pixels (values 0 or 2) are set to 0, and foreground pixels are set to 1, forming a binary mask (mask2). This mask is then applied to the original 16-bit image, extracting the foreground pixel values while setting the background to 0, thereby achieving effective foreground extraction based on the segmentation result.

3.2.1.5 Dilate the Foreground Mask

To expand the boundaries of the target region in the image, we use the dilation operation. It works by applying a structuring element (set as a 3x3 matrix) to the image, which extends the edges of the target region, fills small gaps and connects broken parts, thereby helping to extract a more complete foreground.

3.2.2 Phase image denoising (DMPV)

As shown in Figure 3.2, the phase image denoising process uses the different extracted consistent regions(Figure 3.4) from the magnitude image (Figure 3.3) and records their positions. The position of target region's position is identified as a rectangle with a length of 14 and a width of 10, and the pixel values within this region are recorded. The dynamic thresholding process classifies the top 40% of the regions with the highest mean differences as high-variation regions. The mean difference with the baseline is calculated, and the regions where the difference exceeds a dynamic threshold (shown in Equation 3.7 to Equation 3.10) are replaced with the baseline image. Finally, target position pixels are restored, resulting in a denoised phase image. This approach effectively removes noise while preserving essential phase information.

3.2.2.1 Consistent regions

In phase image denoising, the same preprocessing steps as those for the magnitude image denoising are applied first. Then, the position differences between different bounding boxes are compared and a threshold (tolerance = 2) is applied to determine which bounding boxes are close to each other in the magnitude image. If a bounding box is located near bigger than 20 other bounding boxes, it is considered part of the consistent region. This indicates that this region frequently appears in multiple images. These positions are then mapped to the phase image. As shown in Figure 3.4 (a) and (b) represent consistent regions at different times in the phase image. Duplicating bounding boxes are removed and the final consistent region positions are obtained in the image. The red box highlights the consistent regions.

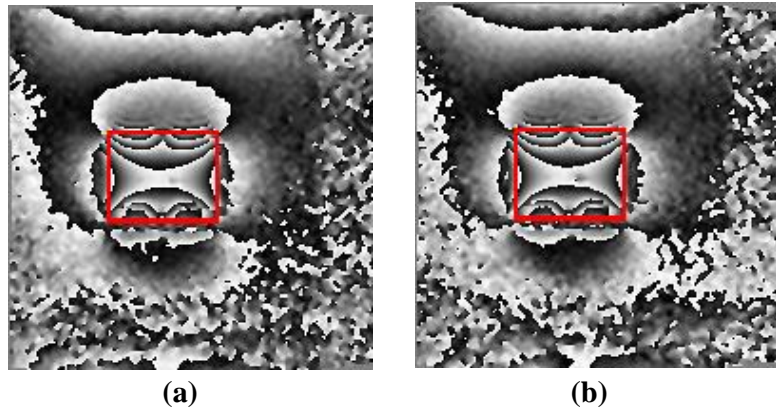


Figure 3.4: The results of consistent region detection marked in red: (a) and (b) represent consistent regions at different times in the phase image.

3.2.2.2 Extract target region

To identify the target region that needs to be protected, the coordinates of the center points of the ROI are first obtained from the magnitude image, and the first ROI is selected as the reference center point. Then, the boundaries of the rectangular region are determined, and the maximum and minimum coordinates of the rectangle are calculated. Finally, all pixel coordinates within the region are recorded and saved to a global list. Based on the coordinates saved in the magnitude image, the corresponding points are marked in the phase image. As shown in Figure 3.5, the results of the target region extraction.

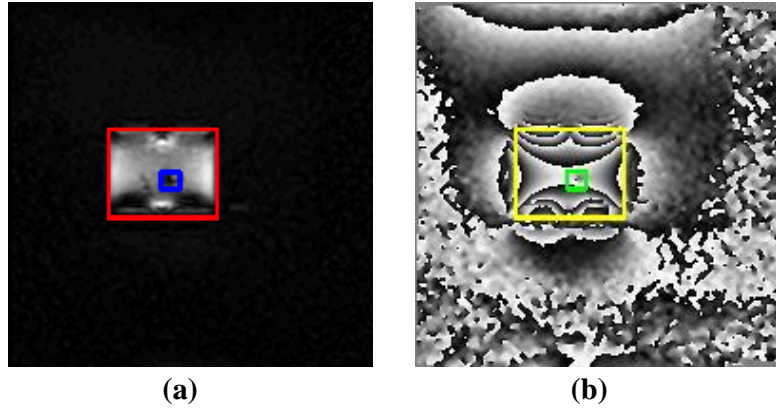


Figure 3.5: The results of target region extraction: (a) consistent region and target region in the magnitude image with the consistent region marked in red and the target region marked in blue. (b) consistent region and target region in the phase image with the consistent region marked in yellow and the target region marked in green.

3.2.2.3 Baseline

(1) Objective evaluation metrics

The Peak Signal-to-Noise Ratio (PSNR) represents the ratio between the maximum signal value and the power of distortion noise that affects the image quality [73], which can be used to assess the SNR of images. The formula for PSNR is as follows:

$$PSNR = 10 \log_{10} \left(\frac{MAX_i^2}{MSE} \right) \quad (3.2)$$

where MSE represents the Mean Squared Error and MAX_i represents the maximum pixel value in the image. A higher PSNR value means better denoised image quality.

The Structural Similarity Index Measure (SSIM) not only focuses on the structural information of images, but also considers brightness, contrast, and fine details in its evaluation [74]. The formula used is as follows:

$$SSIM(x, y) = \frac{(2\mu_x\mu_y + C_1)(2\sigma_{xy} + C_2)}{(\mu_x^2 + \mu_y^2 + C_1)(\sigma_x^2 + \sigma_y^2 + C_2)} \quad (3.3)$$

where μ_x and μ_y represent the mean pixel values of the images x and y . σ_x^2 and σ_y^2 represent their variances. σ_{xy} is the covariance between x and y while C_1 and C_2 are constants. Greater similarity between images is indicated by a higher SSIM value, which corresponds to improved denoised image quality.

(2) Implementation details

The flowchart illustrating the baseline is shown in Figure 3.6.

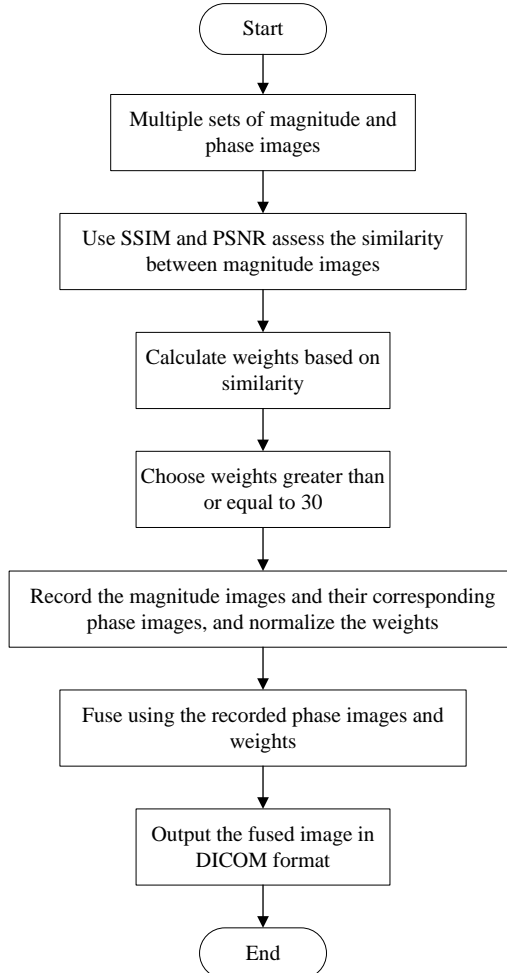


Figure 3.6: The flowchart for the baseline process.

The first three magnitude and phase images are captured in the off-state. First, the first three magnitude images are normalized. Then, SSIM and PSNR are used to assess the similarity between images. The formulas used are as follows:

$$\text{Similarityweight1} = \frac{\text{ssim}_{12} + \text{ssim}_{13}}{2} + \frac{\text{psnr}_{12} + \text{psnr}_{13}}{2} \quad (3.4)$$

$$\text{Similarityweight2} = \frac{\text{ssim}_{12} + \text{ssim}_{23}}{2} + \frac{\text{psnr}_{12} + \text{psnr}_{23}}{2} \quad (3.5)$$

$$\text{Similarityweight3} = \frac{\text{ssim}_{13} + \text{ssim}_{23}}{2} + \frac{\text{psnr}_{13} + \text{psnr}_{23}}{2} \quad (3.6)$$

where Similarityweight1 is the similarity between image1 and image2, and between image1 and image3. $\frac{\text{ssim}_{12} + \text{ssim}_{13}}{2}$ is used to calculate the average SSIM between image1 and image2, and between image1 and image3. $\frac{\text{psnr}_{12} + \text{psnr}_{13}}{2}$ is used to calculate the average PSNR between image1 and image2, and between image1 and image3. The explanation for the other formulas follows the same pattern.

During the weight calculation, magnitude images with weights greater than or equal to 30 are selected for preservation, and their corresponding phase images are also retained. Next, based on the selected weights, the weight of each magnitude image is recorded and normalized. These normalized weights and corresponding phase images are then used to fuse the phase image. The fused image is used as the baseline to replace the noisy areas in the phase images. The result of baseline is shown in Figure 3.7.

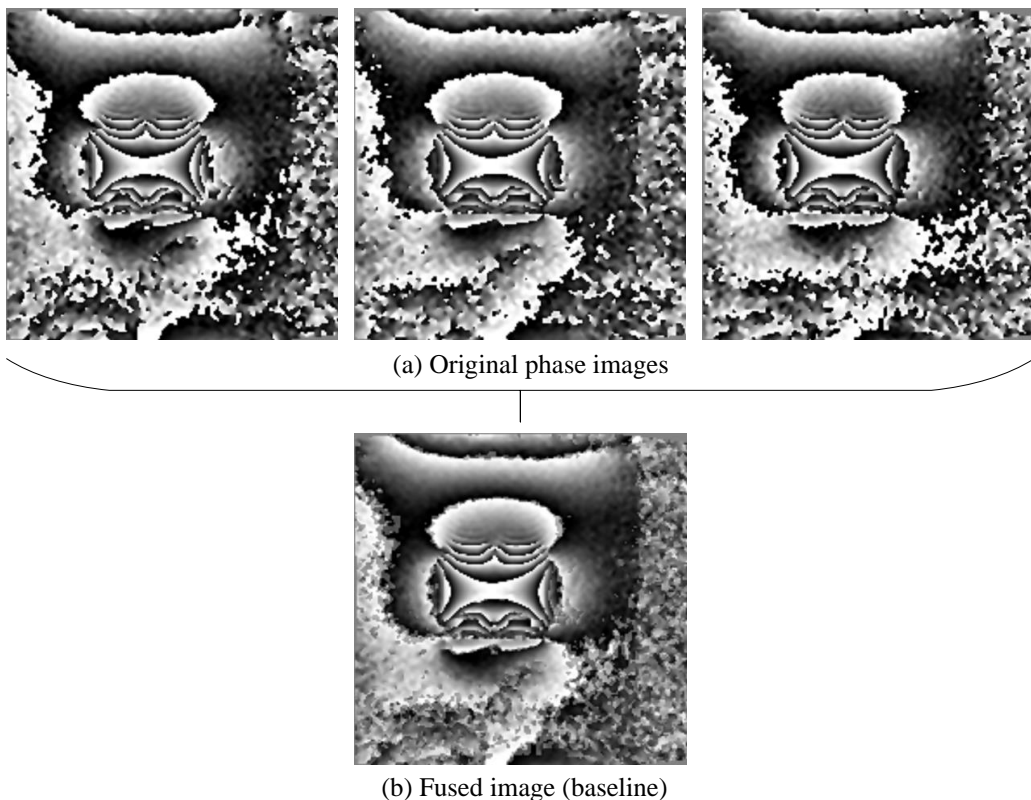


Figure 3.7: The results of baseline: (a) The first three phase images are captured in the off-state. From left to right, they are image1, image2 and image3. (b) Fused image (baseline).

3.2.2.4 Dynamic threshold

This design is based mainly on the mean differences in the consistent regions of the image, applying a dynamic threshold to highlight areas of high variability and denoise by replacing those regions. First, the pixel difference and mean pixel difference between the baseline image and the current image within the consistent regions are calculated. The formulas used are as follows:

$$\text{diff}(x, y) = |\text{baseline}(x, y) - \text{current}(x, y)| \quad (3.7)$$

where $\text{baseline}(x, y)$ is the pixel value in the baseline image. The $\text{current}(x, y)$ is the pixel value in the current image. The $\text{diff}(x, y)$ is the difference value at that point.

$$\text{meanofregion} = \frac{1}{N} \sum_{i=1}^N \text{diff}(x_i, y_i) \quad (3.8)$$

where N is the number of points in the region being analyzed. The $\text{diff}(x_i, y_i)$ represents the absolute difference in pixel values between the baseline and current images at each point (x_i, y_i) . The meanofregion is the mean of the difference values.

Then, the top 40% of the mean differences across all regions are computed, serving as a threshold to distinguish between high and low variation regions. For each region, if the mean difference is greater than or equal to the top 40% value, it indicates a significant change in that region. Next, the standard deviation of the region is calculated and a dynamic threshold is determined. The formula used is as follows:

$$\text{stddiff} = \sqrt{\frac{1}{N} \sum_{i=1}^N (\text{diff}(x_i, y_i) - \text{meanofregion})^2} \quad (3.9)$$

where $\text{diff}(x_i, y_i)$ represents the absolute difference in pixel values between the baseline and current images at each point (x_i, y_i) . The meanofregion is the mean of the difference values. The N is the number of points in the region being analyzed. The stddiff is the standard deviation of the differences.

$$\text{dt} = \text{meanofregion} + \text{stddiff} \quad (3.10)$$

where the dynamic threshold is dt . The mean difference of the region is meanofregion and stddiff is the standard deviation of the differences.

The region is then binarized, setting parts with differences greater than the threshold to white (high variation regions) and others to black. For regions with smaller mean differences, indicating minimal change, no modification is made. Finally, the binarized dynamic thresholding identifies the areas that need to be modified using the baseline. As shown in Figure 3.8, all detected changed regions within the consistent regions are marked in yellow.

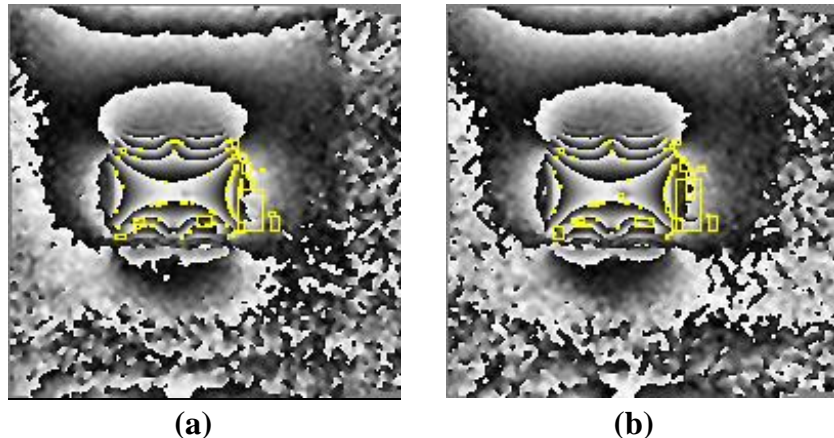


Figure 3.8: All detected changed regions within the consistent regions are marked in yellow.

3.2.2.5 Replace and restore

To extract the contours from the image and update specific regions of the image based on the bounding boxes of the contours, replacing them with corresponding parts from the baseline and protecting target regions. First, external contours are extracted from the image using contour detection. The minimum bounding rectangle for each contour is calculated, obtaining the top-left coordinates, width and height of the rectangle. Next, using this bounding box information, the corresponding regions within the consistent region are replaced with the pixel values from the baseline image, thus updating the region of image. After the replacement is completed, the pixel values of previously protected target region are restored in the image. Specifically, the pixels that need to be protected are first recorded along with their original values. Then, after the image replacement, the stored protected pixels are iterated over and their original values are restored. This ensures that these regions remain unaffected by the replacement operation, thereby maintaining their integrity and accuracy.

3.3 Hampel–Gaussian

To further assess the temperature state of the target tissue and reduce misjudgments caused by errors, this paper proposes a Hampel–Gaussian method, which combines a Hampel filter for detecting outliers with a Gaussian trinomial model for temperature profile smoothing to repair them.

As shown in Figure 3.9, the flowchart describes the process of outlier handling. First, outliers are detected using the Hampel filter. Next, Gaussian trinomial model is applied to repair individual outliers. Then, segments containing more than three outliers within 20 seconds are detected and processed. Furthermore, special treatment is applied to outliers in the peak area. The entire method fits the data using the Gaussian trinomial formula and corrects any detected outliers.

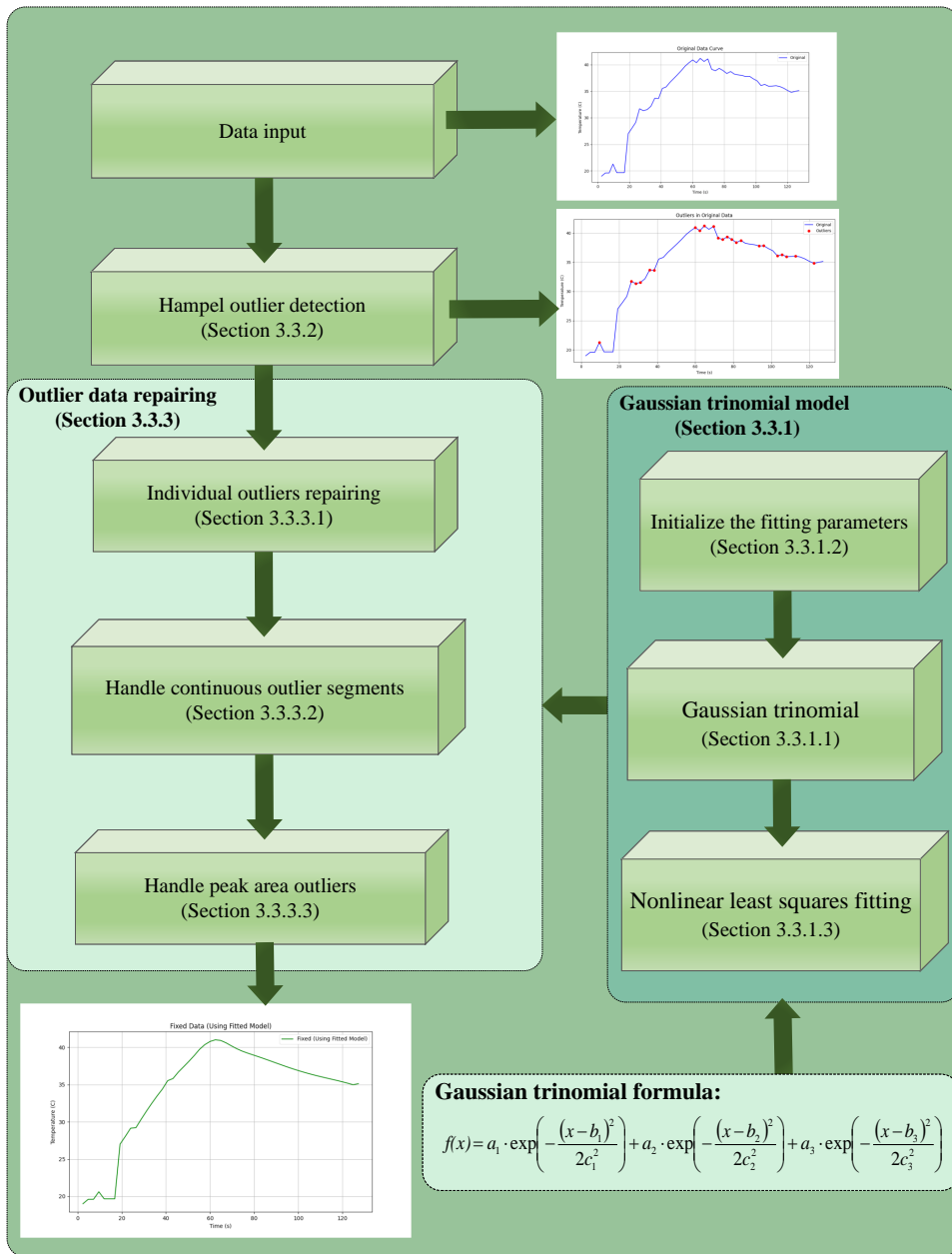


Figure 3.9: The flowchart of the temperature profile smoothing process.

3.3.1 Gaussian trinomial model

3.3.1.1 Gaussian trinomial

We define a Gaussian trinomial function. The formula used is as follows:

$$f(x) = a_1 \exp\left(-\frac{(x-b_1)^2}{2c_1^2}\right) + a_2 \exp\left(-\frac{(x-b_2)^2}{2c_2^2}\right) + a_3 \exp\left(-\frac{(x-b_3)^2}{2c_3^2}\right) \quad (3.11)$$

where the a_1 , a_2 and a_3 represent the amplitudes of the respective Gaussian components. The b_1 , b_2 and b_3 represent their means. The c_1 , c_2 and c_3 represent their standard deviations.

To achieve accurate and rapid fitting of the Gaussian trinomial model in subsequent steps, we use K-means

clustering to obtain initial parameter estimates which is introduce in subsubsection 3.3.1.2. Nonlinear least squares fitting to fit the temperature profile.

3.3.1.2 Initialize the fitting parameters

The K-means clustering algorithm is used to cluster the given data and initialize the fitting parameters for a Gaussian trinomial model. By applying the K-means algorithm to the input data X , the data is divided into three clusters and the centroids of each cluster are determined. Each centroid represents the center of a cluster and is used to estimate the initial parameters of the Gaussian distributions.

After clustering, the amplitude a_1 of the first Gaussian distribution is calculated by determining the range of the temperature data, which is the difference between the maximum and minimum values of the data. Meanwhile, a_2 and a_3 are scaled by preset factors of 0.8 and 0.5.

Next, the centroids obtained from K-means clustering are used to estimate the means of the three Gaussian distributions. The centroids provide the central positions of the clusters, so the values from the first column of the centroid matrix are assigned to b_1 , b_2 and b_3 , which serve as the initial means for the three peaks.

Additionally, the standard deviation of the temperature data is calculated and used to estimate the volatility of each Gaussian distribution. The standard deviation indicates the dispersion of the data. A larger standard deviation means the data is more spread out, while a smaller standard deviation indicates that the data is more concentrated. By multiplying the standard deviation by different preset factors (0.2, 0.5 and 0.9), the initial standard deviations (c_1 , c_2 and c_3) for each Gaussian distribution are obtained.

3.3.1.3 Nonlinear least squares fitting

To adjust the model parameters, we use nonlinear least squares fitting to ensure that the predictions of Gaussian trinomial model are as close as possible to the actual data, thereby finding the optimal model parameters. This method primarily works by minimizing the squared error between the predicted values of model and the actual data to find the best-fit parameters. We set the maximum number of function evaluations to 10,000 to improve the optimization performance in complex fitting processe. To assess the precision of parameter estimates, we use the parameter covariance matrix, which provides uncertainty information about the fitted parameters. When using nonlinear least squares fitting, we usually need to provide some initial guess values (subsubsection 3.3.1.2), which serve as the starting point for the optimization algorithm. A reasonable initial guess plays a crucial role in the convergence speed and final accuracy of the optimization process.

Figure 3.10 shows the result of the Gaussian trinomial model fitting profile in (a) and (b). The blue line represents the original profile while the red line represents the fitted profile.

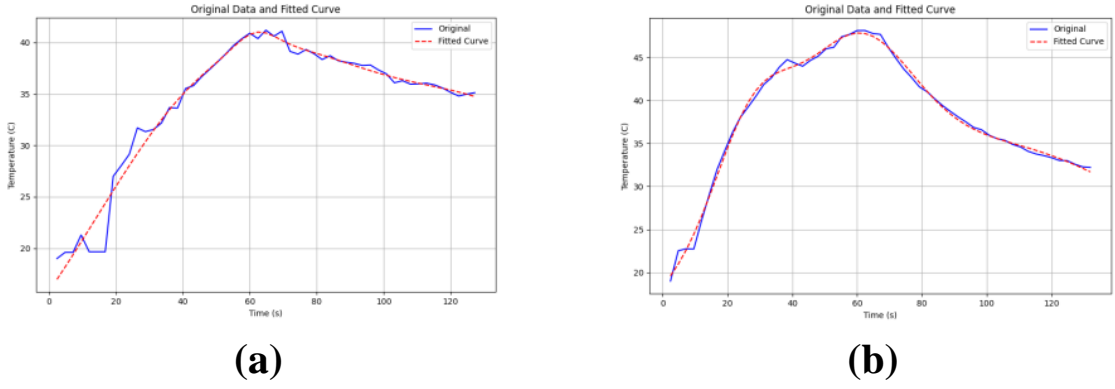


Figure 3.10: The result of Gaussian trinomial model fitting profile in (a) and (b). The blue one represents original and the red one is fitted profile.

3.3.2 Hampel outlier detection

Based on the Hampel filter for outlier detection, the method traverses the data using a fixed sliding window of size 7. For each window, the median and the median absolute deviation (MAD) are computed. A data point is classified as an outlier if its deviation from the median of the window exceeds a preset threshold. The preset threshold is defined as:

$$\text{Threshold} = \sigma \cdot 1.4826 \cdot \text{MAD} \quad (3.12)$$

where σ typically denotes the threshold factor and we set it to 0.01. The constant 1.4826 is used to approximate the conversion between MAD and the standard deviation. MAD is generally calculated from a data window by first determining the median of the values in that window, then taking the absolute difference of each point from that median and finally computing the median of these absolute differences.

Figure 3.11 shows the result of Hampel outlier detection applied to the original data. (a) displays the temperature profile drawn using the original data, while (b) highlights the detected outliers in the original data with red dots.

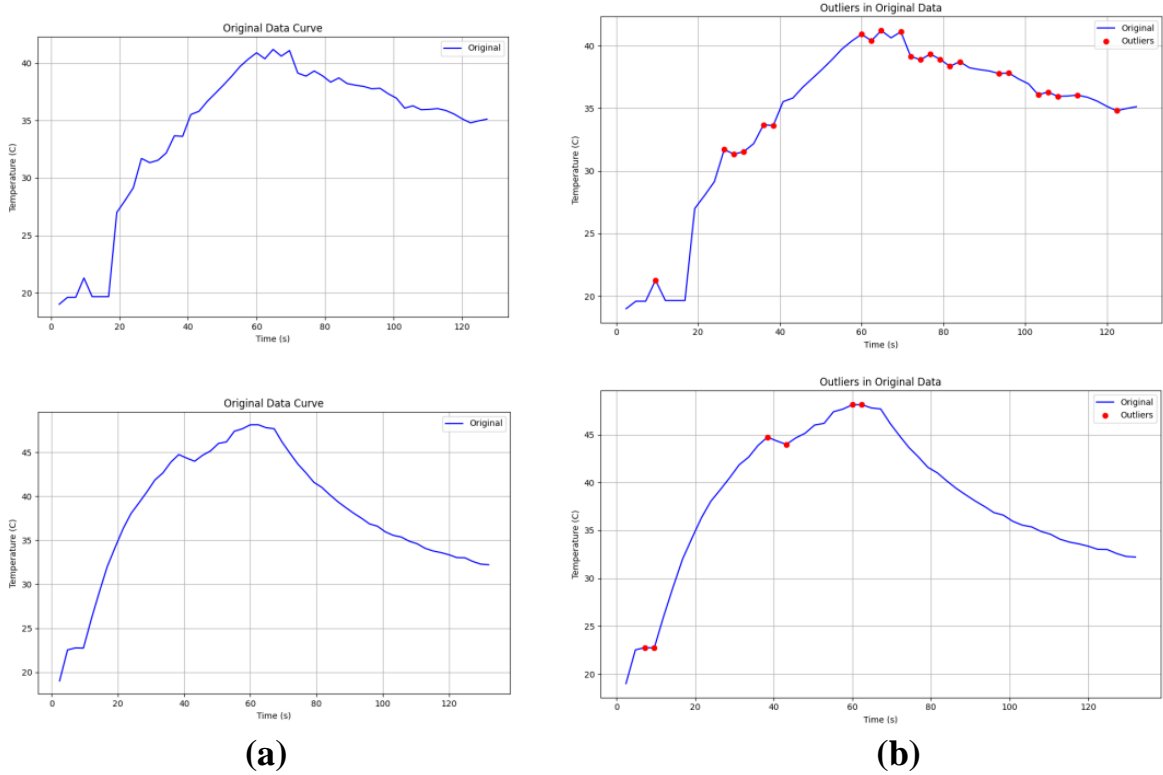


Figure 3.11: The result of the Hampel outlier detection: (a) use original data to draw a profile. (b) outliers detect in original data.

3.3.3 Outlier data fixing

3.3.3.1 Handle Individual outliers

The optimal parameters obtained are passed as individual arguments to the Gaussian trinomial model. By using these optimal parameters, the model computes the predicted temperature value for each individual outlier.

3.3.3.2 Handle continuous outlier segments

To eliminate abnormal fluctuations, we traverse each outlier and search for consecutive outlier segments within 20 seconds. If a segment contains more than two outliers, the original data of that segment is replaced with the Gaussian trinomial model fitted data.

3.3.3.3 Handle outliers in the peak area

To avoid incorrectly modifying the peak region, the peak position is first detected and determined. Then, outliers within 16 seconds before and after the peak are identified. If the number of outliers is less than or equal to 2, the original data values are used to replace the outliers in this segment, thereby preventing erroneous adjustments to the peak region. As shown in Figure 3.12, it is the results of peak area outlier handling.

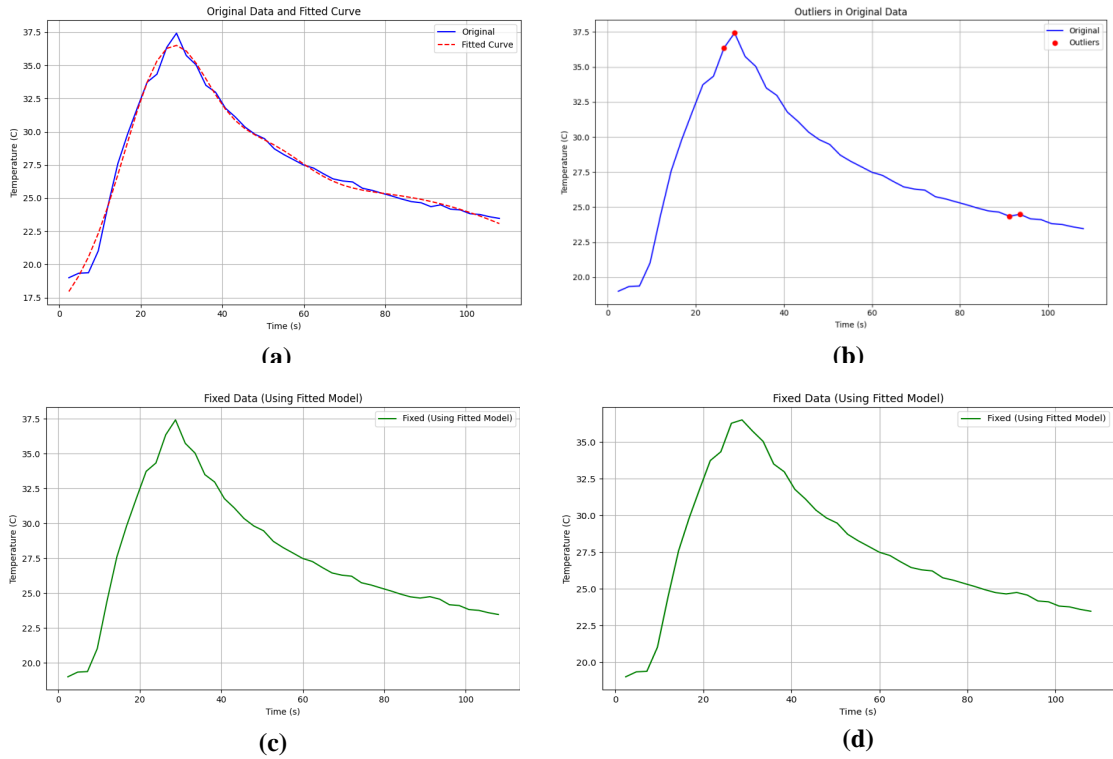


Figure 3.12: The results of peak area outlier handling.(a) displays the original data along with the Gaussian trinomial model. (b) highlights the outliers, which are marked with red dots. (c) shows the result after applying the peak area outlier handling method and (d) shows the result without using the method.

3.4 Custom methods developed for comparison

3.4.1 Heat map denoising

Figure 3.13 shows the process and the result of custom heat map denoising. We use the YOLO model to detect the target areas and apply Hue, Saturation and Value (HSV) to remove noise and use inpainting in the non-target regions. This method effectively preserves the target areas in the image as well as the color bar. First, the pretrained YOLO model is loaded which is used to predict and generate bounding boxes around the target areas(Figure 3.13 (a)). Then, for the regions outside the target areas, the red and yellow ranges in the HSV color space are defined to create a mask that removes these color noise (Figure 3.13 (b)) while ensuring that the color bar area is excluded from the processing. As shown in Figure 3.13 (c), we use diffusion-based inpainting method to inpaint the image.

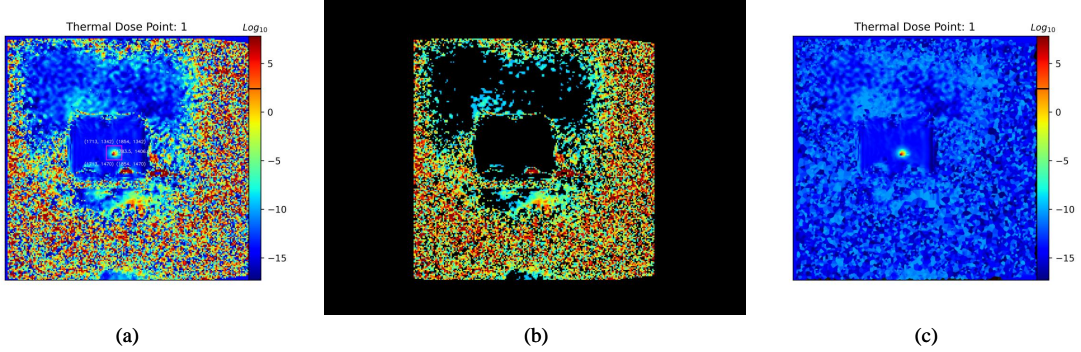


Figure 3.13: The process and the result of custom heat map denoising: (a) the image shows the YOLO model detecting target areas. (b) use HSV to extract noise. (c) the result of heat map denosing.

3.4.2 Temperature profile smoothing

3.4.2.1 The first comparative method

The first comparative method involves extracting blue profile data from images, detecting outliers and correcting them. The process begins by loading the input image, segmenting blue regions using the HSV color space and extracting the pixel coordinates of the profile, which are then mapped to actual time and temperature data. Subsequently, multiple anomaly detection methods are applied for comprehensive analysis, including global anomaly detection based on Z-scores, local anomaly detection using multi-scale sliding windows and special point detection based on zero slopes. These methods complement one another, collectively identifying anomalies within the temperature profile. The detected anomalies are corrected using interpolation to ensure smoothness and continuity in the profile data.

As shown in Figure 3.14, this shows the results of the first custom temperature profile smoothing process. In (a), the left images in each row display the original temperature profiles, where noticeable fluctuations or abrupt changes occur at certain moments. In (b), the temperature data is corrected using the first comparative method and the resulting smoothed profiles exhibit a more stable trend. In (c), the detected outliers are marked on the original data profile with red dots.

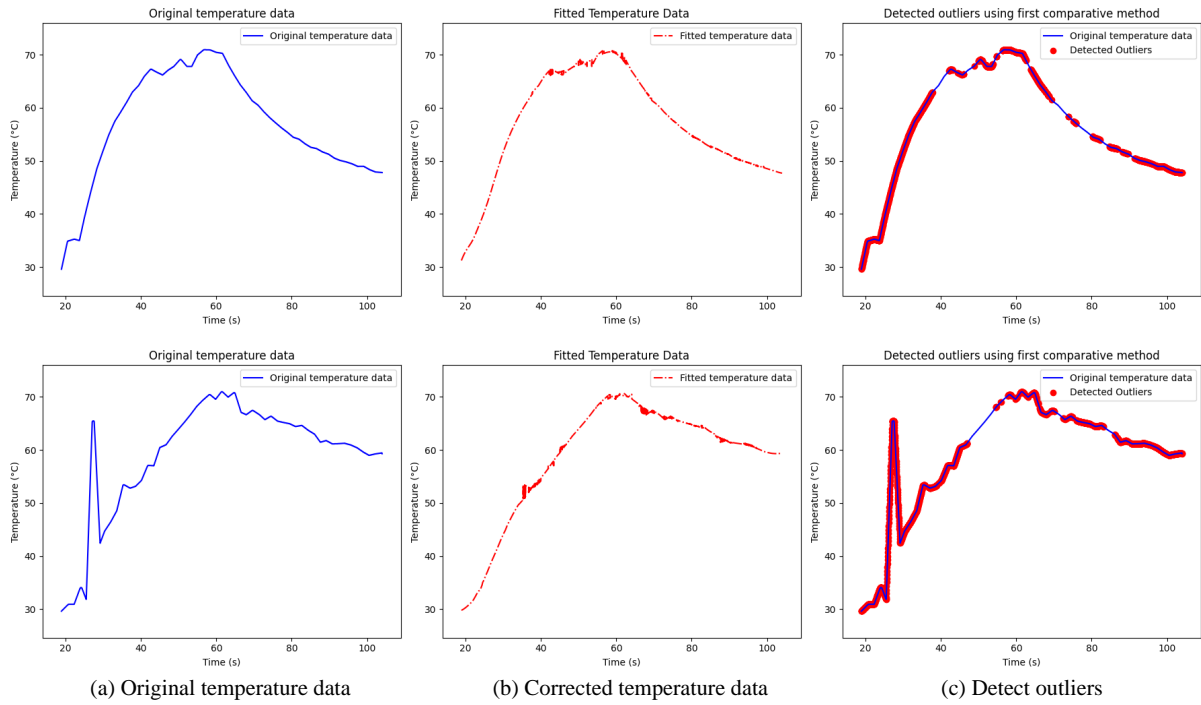


Figure 3.14: The process and the result of the first custom profile smoothing: (a) the image shows original temperature data. (b) use the first comparative method to correct. (c) the result of outliers detection.

3.4.2.2 The second comparative method

The second comparative experiment uses a profile fitting method. MATLAB is used to fit a profile that aligned closely with the observed trend. Figure 3.15 is MATLAB fitted profile aligned with the observed trend.

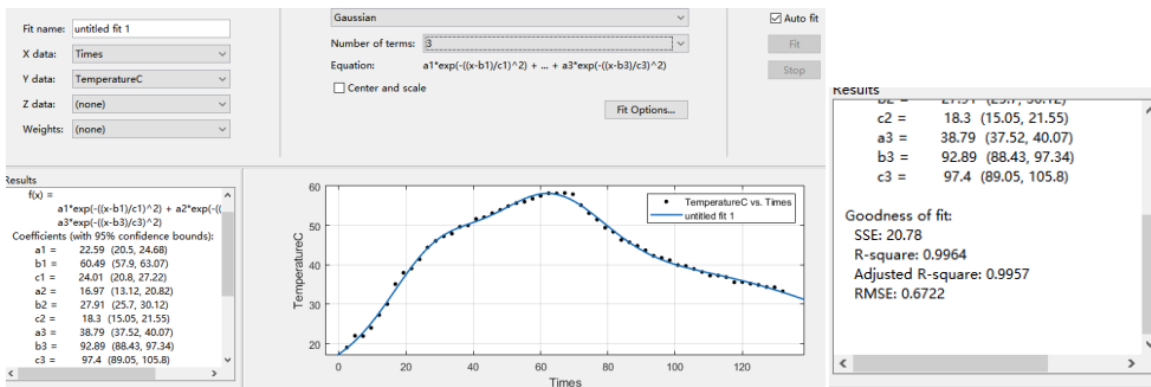


Figure 3.15: MATLAB fitted profile aligned with the observed trend.

Based on this experiment, the following formula is determined:

$$f(x) = a_1 \exp\left(\frac{-(x-b_1)^2}{c_1^2}\right) + a_2 \exp\left(\frac{-(x-b_2)^2}{c_2^2}\right) + a_3 \exp\left(\frac{-(x-b_3)^2}{c_3^2}\right) \quad (3.13)$$

where a_1-a_3 represent the amplitude of each Gaussian distribution, determining the peak height. The b_1-b_3 represent the peak position, defining the center of the Gaussian peak. The c_1-c_3 indicate the standard deviation, controlling the width and shape of each Gaussian peak.

As shown in Figure 3.16, it shows the results of the second custom profile smoothing process with Gaussian model fitting method.

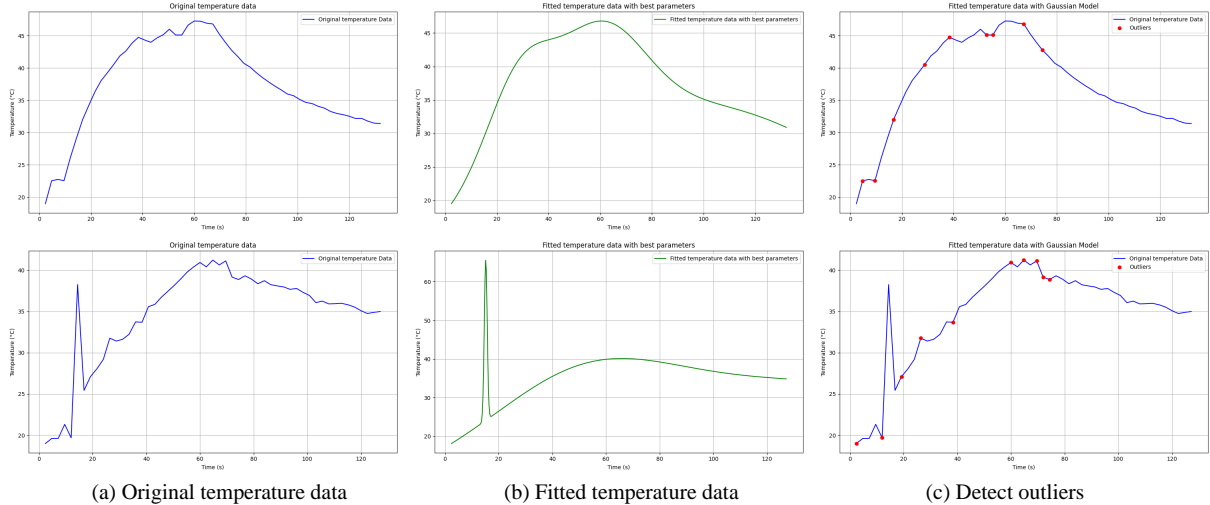


Figure 3.16: The process and the result of the second custom profile smoothing: (a) the image shows original temperature data. (b) use the second comparative method to correct. (c) the result of outliers detection.

4 Experimental Results

4.1 Setting and Description

MRgFUS images were captured using the Siemens Magnetom Vida system with 3T magnetic field strength (Siemens, Limassol, Cyprus). The therapeutic transducer was developed in-house using non-magnetic materials selected based on simulation results to ensure optimal focusing at sufficient tissue depth. It features a compact, ergonomic design with a single piezoelectric element (2.75MHz, 50mm diameter, 65mm curvature radius) housed in a custom ABS case. The transducer is driven by a tuned RF amplifier (AG1016, T&C Power Conversion, Inc.) for maximum power gain, achieving an average efficiency of approximately 30% [75].

To evaluate the effectiveness of the proposed denoising method, we compare it with traditional denoising methods and deep learning model. Traditional methods include Gaussian filter [28], Bilateral filter [30], NLM [33] and TV [38]. Deep learning model includes YOLO-HSV which is a custom method developed for comparison.

To evaluate the effectiveness of the proposed temperature profile smoothing method, we compare it with traditional methods. Traditional methods include LOESS [60] and two custom method developed for comparison in subsection 3.4.2.

The experiments are conducted on a cloud server equipped with an Intel(R) Xeon(R) Platinum 8336C CPU and dual RTX 2080 Ti GPUs (22GB).

4.2 GB-DMPV

For the denoising experiments, the HIFU acoustic parameters are configured as follows: for the first, third and fourth images in Figure 4.1 and Figure 4.2, power = 300W, time on = 60s, time off = 60s and frequency = 2.75MHz. For the second image, the parameters are: power = 200W, time on = 30s, time off = 60s and frequency = 2.75MHz.

4.2.1 Visual Effects

Figure 4.1 illustrates the results of heat map denoising, with the first row showing the noisy heat maps and the second to seventh rows showing the denoised heat maps, which are processed using Gaussian Filter (b), Bilateral Filter (c), Non-Local Means (NLM) (d), Total Variation Denoising (TV) (e), Custom methods developed for comparison (YOLO-HSV) (f) and the method proposed(GB-DMPV) (g). As shown in (a), the noisy images exhibit significant color interference, which severely affects the recognition and analysis of target areas, especially the third image. These interferences could be caused by instrument noise or environmental factors. The noise creates a chaotic appearance, making it difficult to distinguish real heat spots from irrelevant random disturbances. In some cases, particularly low thermal doses and the edges of the tissue, large patches of noise further obscure the smooth transition layers of thermal diffusion. In contrast, the denoised results in (b), (c), (d) and (e) show minimal improvement,

with many remaining disturbances that still affect the accuracy and could lead to mislead clinical analysis. In comparison, the YOLO-HSV method shown in (f) effectively removes interference color blocks in non-target areas by combining the YOLO model to detect the target areas and performing noise removal in the HSV space, preserving the target information while effectively reducing background noise. The denoised heat maps show a significant reduction in background noise, resulting in smoother and more uniform backgrounds. Many of the red or yellow noise spots visible in the noisy heat maps are eliminated, and the high-dose areas in the denoised images are more prominent and clearly defined. However, some interference is introduced. Finally, GB-DMPV (g) shows the results of the proposed method, which can effectively remove noise while preserving the target areas. This method performs more stably in complex noisy backgrounds and can highlight the target areas more effectively.

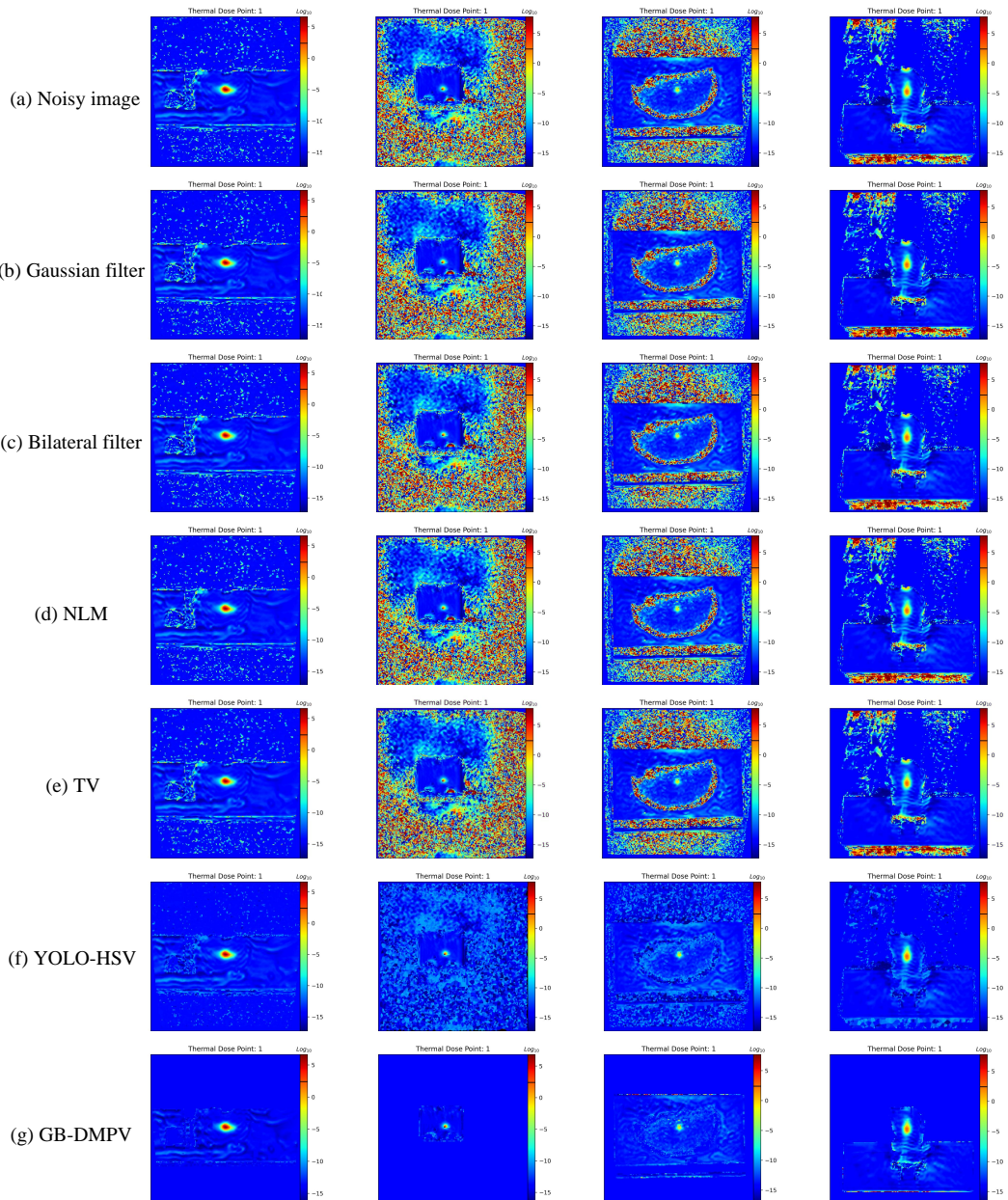


Figure 4.1: The results of heat map denoising:(a) Noisy image, (b) Gaussian filter, (c) Bilateral filter, (d) NLM, (e) TV, (f) YOLO-HSV and (g) GB-DMPV.

4.2.2 Ablation Study

Figure 4.2 shows the ablation experiment results of heat map denoising. (a) is the noisy heat map, (b) is fixed GB, (c) is fixed DMPV, and (d) is GB-DMPV. To validate the effectiveness of the GB-DMPV method in heat map denoising, (b) Fixed GB and (d) GB-DMPV are compared to verify the role of DMPV, while (c) Fixed DMPV and (d) GB-DMPV are compared to verify the role of GB.

As shown in Figure 4.2, (a) is the original noisy heat map, which contains a significant amount of interference noise, especially in low thermal areas and at the edges of the tissue. These noises are typically caused by instrument errors, environmental interference, and other factors, resulting in random color spots areas in the image, which complicates heat map analysis. In this image, we can clearly observe the chaotic noise in the background, which affects the identification of the high thermal regions, especially the third image in noisy image (a). As the transition layers around the thermal spots are covered by this noise, making it difficult to observe the smooth transition of thermal diffusion. Fixed GB (b) shows the background noise has been removed, but some larger noise remains, especially in the third image. Fixed DMPV (c) shows some noise has been removed, there are still noticeable noise in the background, particularly in low thermal areas. GB-DMPV (d) significantly reduces the background noise in the image, especially in the thermal spot and low-dose areas. The noise removal effect is particularly noticeable. The image becomes smoother and more uniform, with the contours of the thermal spots being more distinct and prominent. This method effectively removes all unnecessary noise while preserving the details of the target areas, demonstrating a clear advantage in denoising.

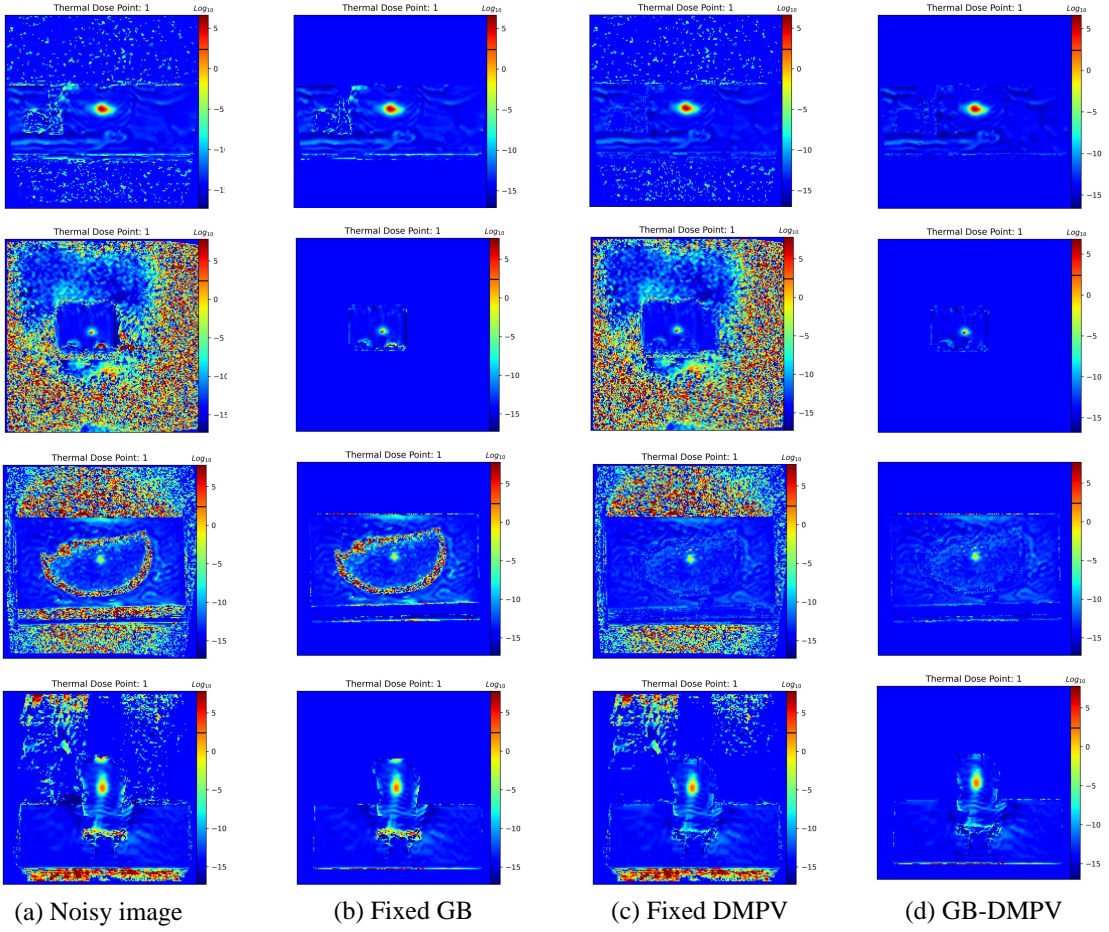


Figure 4.2: Visual comparisons of heat map denoising methods in ablation study: (a) Noisy image, (b) Fixed GB, (c) Fixed DMPV, (d) GB-DMPV.

4.2.3 The Effect of Denoising on the Temperature Profile

Figure 4.3 consists of two columns. (a) shows the temperature profile before denoising and (b) shows the temperature profile after denoising. As shown in Figure 4.3 (a), before denoising, the temperature shows significant fluctuations at certain moments. In Figure 4.3 (b), after denoising, large fluctuations are removed, profiles become smoother and make overall trend more coherent. The profiles in the right column have smaller fluctuations compared to those in the left column, and the number of outliers is significantly reduced. In the first row of Figure 4.3, the original data presents a declining fluctuation. After applying the denoising algorithm, the profile becomes much smoother, with the temperature changes becoming more stable and without sharp spikes, trending towards a steady change. In the second row, fluctuations still appear, especially in the rising temperature portion, where temperature undergoes abrupt changes within a certain range. After denoising, the data tends to be smoother, abnormal fluctuations are reduced and noticeable jump points are removed. In the third row, the original data shows significant sharp fluctuations, with temperature changing in a long time and the profile exhibits noticeable jumps with prominent outliers. After denoising, the temperature profile become smoothing. However, there are still some fluctuations remain. In the fourth row, the profile before denoising shows large fluctuations, with dramatic changes in the temperature profile. After denoising, the profile becomes relatively smooth,

with the fluctuations significantly suppressed, making the overall trend more coherent.

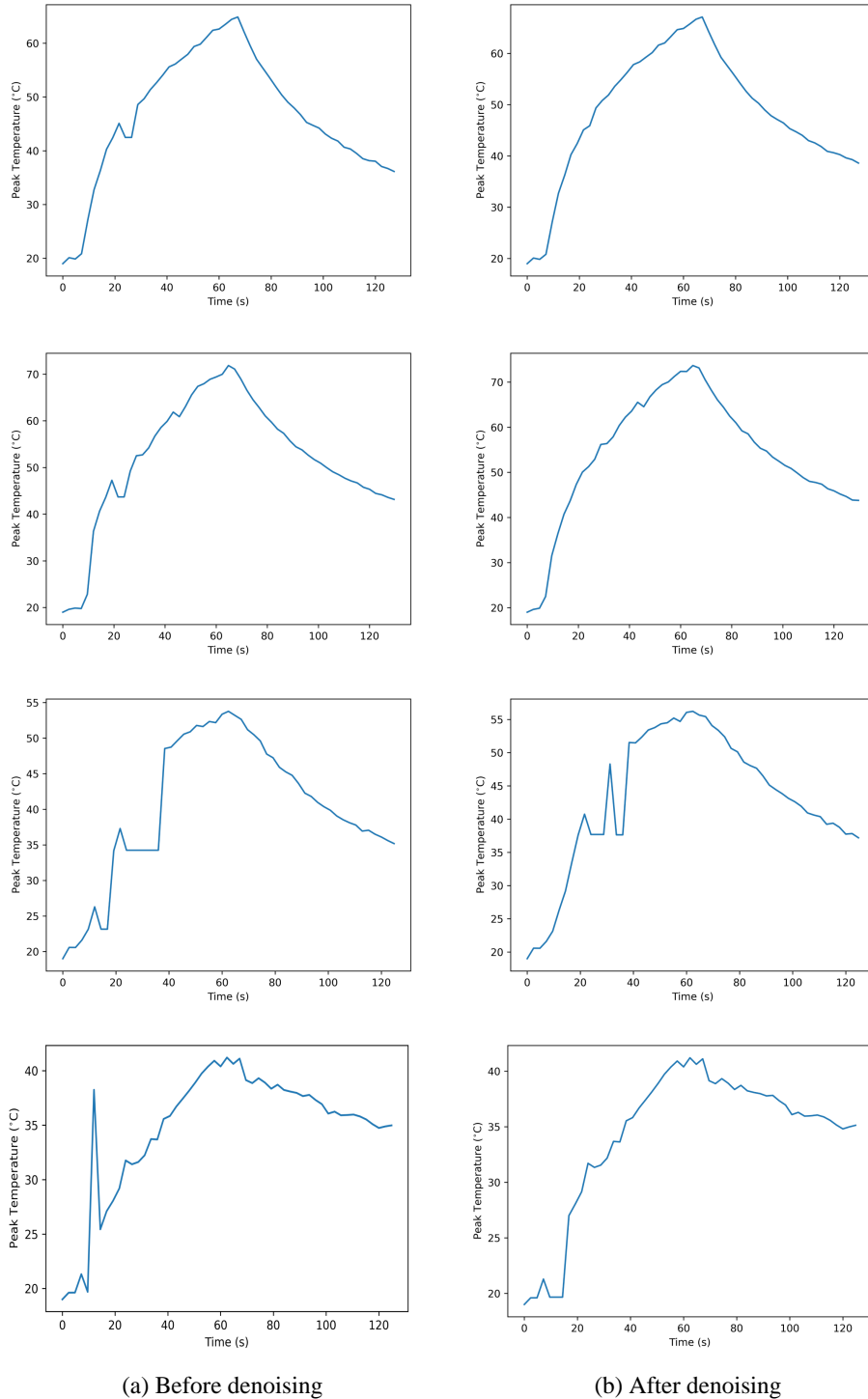


Figure 4.3: The result of the effect of denoising on the temperature profile. (a) the temperature profile before denoising and (b) the temperature profile after denoising.

After denoising, the temperature profile becomes relatively smooth and no longer shows obvious spikes or fluctuations except the third one. In fact, the third temperature profile reduces fluctuations to some

extent and restores part of the values affected by interference. This indicates that the denoising algorithm effectively removes external interference and noise, making it easier to identify important temperature changes during the treatment process. This provides doctors with more reliable decision-making support. With the denoised temperature data, it becomes clearer to observe the heating trend of the target tissue, ensuring precise control of the treatment area and avoiding tissue damage caused by excessive or insufficient heating.

4.2.4 Summary

The results of the heat map denoising experiments demonstrate a comparison of various denoising methods. From the visual comparison of different methods, it is evident that traditional methods such as Gaussian filter, bilateral filter, NLM and TV show limited denoising effects. The YOLO-HSV method, by combining object detection and noise removal in the HSV color space, performs better in preserving target information while removing non-target noise. However, the proposed GB-DMPV method significantly outperforms all other methods in terms of preserving target areas and removing background noise. This method excels in complex noisy environments and highlights the target regions more clearly and stably.

The ablation study further confirms the superiority of the GB-DMPV method. Compared with Fixed GB and Fixed DMPV, the GB-DMPV method performs excellently in noise removal. This method effectively preserves the contours of thermal spots while eliminating background noise, making it the most effective denoising method in this study.

Additionally, the denoising process significantly improves the temperature profiles. The comparison of temperature data before and after denoising shows smoother and more stable trends, reducing some outliers and fluctuations. The enhanced stability of temperature data helps accurately identify key temperature changes during treatment, ensuring precise control of heating in target tissues, thus reducing the risk of tissue damage caused by overheating or underheating.

4.3 Hampel–Gaussian

4.3.1 Comparison of Visual Effects in Experiment

Figure 4.4 shows the comparison of different temperature profile smoothing methods. The original temperature data (a) shows unprocessed profiles that fully preserve the fluctuations and abrupt changes in the data. The LOESS (b) smoothing method uses a locally weighted regression model by applying weighted least squares to fit each data point and its neighborhood, thereby achieving temperature profile smoothing. The figure shows that LOESS removes most abrupt changes, making the overall temperature profile smoother. However, this method also has some issues: (1) After smoothing, the originally sharp peaks need to be protected are lowered. (2) In some images, the peak positions shift relative to the original data. In particular, in the fourth image, where the original data shows only one peak, LOESS produces two peaks with significantly reduced heights. The first comparison method (c) fits results generally match the original data in the first three temperature profiles, despite some repeated fitting. However, in the fourth image, the peak position becomes abnormal and the vertical axis readings do not correspond with

those of the original temperature profile. The second comparison method (d) uses a Gaussian model for fitting, which achieves smooth transitions. However, it also shows problems in the fourth image, the peak height is significantly reduced, resulting in excessive smoothing and a loss of some details. The Hampel–Gaussian method (e) effectively removes outliers while better preserving the details of the temperature profile. The overall profile exhibits moderate smoothness that more closely reflects the true trend of the original data. This method achieves a good balance between smoothing abrupt changes and fluctuations while retaining important details.

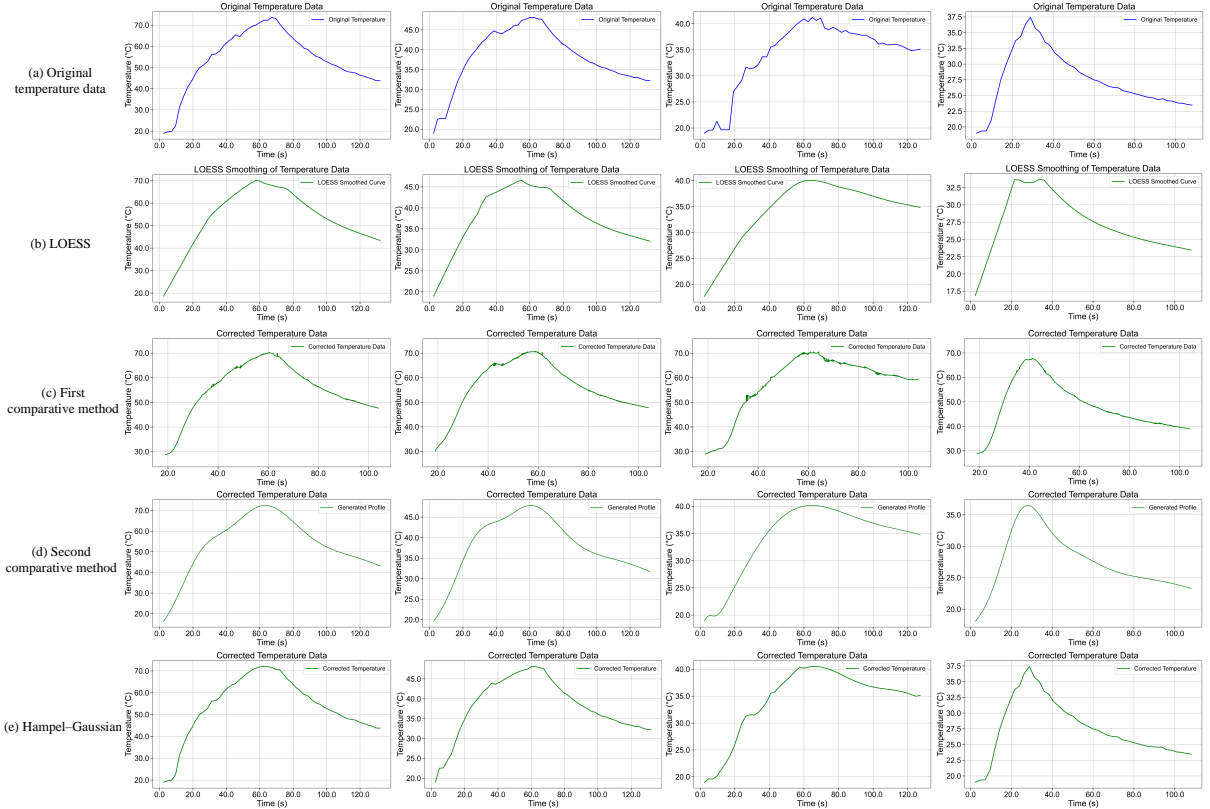


Figure 4.4: The result of temperature profile smoothing. (a) original temperature data, (b) LOESS, (C) the first comparative method which is introduced in subsubsection 3.4.2.1, (d) the second comparative method which is introduced in subsubsection 3.4.2.2 and (e) Hampel–Gaussian.

4.3.2 Outliers with different data repairing

Figure 4.5 shows the results of an ablation study in the data repair process, demonstrating the impact of different processing methods on the data repair effect through four different images. Remove outlier segments process compares with Hampel–Gaussian to demonstrate the effect of retaining the treatment for anomalous segments. Remove peak region process compares with Hampel–Gaussian to demonstrate the effectiveness of retaining the treatment for the peak region.

As shown in Figure 4.5 (a), the original temperature data is displayed, which shows significant fluctuations. Figure (b) effectively removes most of the anomalies and makes the temperature profile appear much smoother and more in line with expectations. In figure (c), the effect of repairing the data after removing the outlier segments is shown. Compared with method (b), the repaired temperature profile still shows fluctuations and anomalies, particularly in the first image of (c), where a downward trend is

observed. Finally, figure (d) displays the effect of repairing the data after removing the treatment of the peak region. Actually the peak is not an anomaly in the second image of (d), and the failure to retain the smoothing leads to a temperature loss.

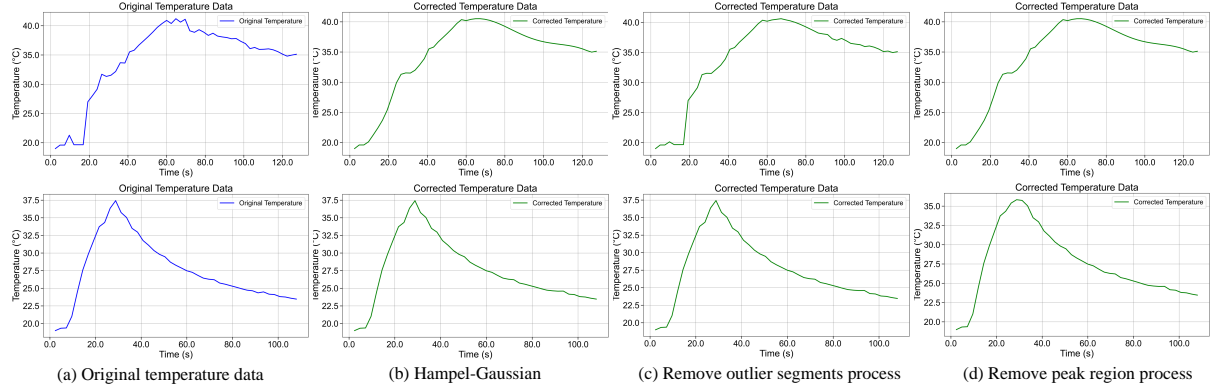


Figure 4.5: The result of outliers with different data repairing: (a) Original temperature data, (b) Hampel–Gaussian, (C) Remove outlier segments process and (d) Remove peak region process.

4.3.3 Summary

The experimental results in Figure 4.4 and Figure 4.5 highlight the advantages of the Hampel-Gaussian method in temperature profile smoothing. In Figure 4.4, the Hampel-Gaussian method combines Hampel filter with Gaussian trinomial smoothing, effectively removing most outliers while preserving the details of the temperature profile. This allows the temperature profile to smooth out abrupt changes and fluctuations while still reflecting the overall trend of the original data. Compared with other methods, the Hampel-Gaussian method balances fluctuations removal and detail preservation while retaining key data features.

The Outliers with different data repairing in Figure 4.5 further validates the effectiveness of the Hampel-Gaussian method. Compared with other data repair methods, the Hampel-Gaussian method better smooths the data, removes outliers and results in a temperature profile that more closely matches expectations.

Overall, the Hampel-Gaussian method demonstrates superior performance in temperature profile smoothing.

5 Discussion

The two methods proposed in this study, GB-DMPV for heat map denoising and Hampel-Gaussian for temperature profile smoothing, significantly improve the accuracy and reliability of temperature measurements in MRgFUS therapy.

5.1 Effectiveness of GB-DMPV in Heat Map Denoising

The GB-DMPV method combines the GrabCut with automatically detects and adaptively modifies phase variations to address noise issues in heat map images. By using GrabCut to segment target regions while preserving structural details, this method effectively reduces noise without blurring critical features. The integration of dynamic thresholding and baseline fusion further optimizes the denoising process, especially in high-variation regions. Experimental results (Figure 4.1) show that GB-DMPV outperforms traditional filters (such as Gaussian, bilateral filters, NLM and TV) and deep learning-based methods (such as YOLO-HSV). For example, GB-DMPV not only removes noise but also retains sharp thermal dose contours, which is crucial for real-time clinical decision-making.

5.2 Advantages of Hampel-Gaussian in Temperature Profile Smoothing

The Hampel-Gaussian method addresses the fluctuations caused by outliers in temperature data. By combining Hampel filter for outlier detection and a Gaussian trinomial model for temperature profile smoothing, this method achieves a good balance between fluctuations removal and trend preservation. As shown in Figure 4.4, Hampel-Gaussian outperforms LOESS and other comparison methods by effectively reducing peak distortion and preventing over-smoothing. This is particularly important in MRgFUS therapy, where abrupt temperature changes must be accurately monitored to avoid tissue damage.

The improved denoising and smoothing techniques remove noise in heat map images and stabilize temperature profiles, clinicians can better assess treatment effectiveness and adjust parameters in real time. Despite the many advantages of this study, there are still some limitations. While GB-DMPV shows promising results, its computational complexity (iterative GrabCut optimization) may limit real-time processing capabilities in high-throughput clinical environments. The Gaussian trinomial model assumes a specific distribution, which may not fully capture the heterogeneity of temperature fluctuations.

6 Conclusion

This study addresses the challenges of noise interference in heat map images and fluctuations in temperature profiles during MRgFUS therapy. Two novel methods are proposed to enhance the accuracy and reliability of MR thermometry: GB-DMPV for heat map denoising and Hampel-Gaussian for temperature profile smoothing. The GB-DMPV method combines the GrabCut algorithm with automatically detects and adaptively modifies phase variations, effectively removing noise while preserving critical target areas in the heat map. It outperforms traditional denoising methods and deep learning-based technique, especially in complex noisy environments. In terms of temperature profile smoothing, the Hampel-Gaussian method combines Hampel outlier detection with a Gaussian trinomial model, effectively identifying and repairing anomalies in the temperature profile, while avoiding over-smoothing of critical temperature trends. This method achieves a good balance between fluctuations removal and detail preservation.

Experimental results show that GB-DMPV significantly improves the clarity of heat maps, removes noise and enhances the visibility of high thermal dose regions. Ablation study confirms the importance of GB-DMPV for optimal performance. The Hampel-Gaussian method effectively removes outliers while preserving the physiological relevance of temperature trends. It can handle continuous outlier segments and peak regions, ensuring the reliability of the data, making it suitable for clinical decision-making.

The proposed methods provide effective technical support for real-time temperature monitoring during MRgFUS treatments, enabling precise control of thermal ablation and reducing the risk of over-treatment or under-treatment. By smoothing temperature profiles and providing clearer heat maps, these methods offer more reliable clinical data, improving treatment safety and efficacy. However, the performance of GB-DMPV is still influenced by the consistent region detection and may degrade when the target tissue is visually similar to the surrounding background. The Hampel-Gaussian method assumes the parameters of the Hampel filter (such as window size and threshold) are manually set. Future work could integrate deep learning methods to detect consistent regions, achieve automatic parameter adjustment in dynamic environments and validate the approach with larger clinical datasets.

BIBLIOGRAPHY

- [1] P. E. Huber, J. W. Jenne, R. Rastert, I. Simiantonakis, H.-P. Sinn, H.-J. Strittmatter, D. von Fournier, M. F. Wannenmacher, and J. Debus, “A new noninvasive approach in breast cancer therapy using magnetic resonance imaging-guided focused ultrasound surgery,” *Cancer research*, vol. 61, no. 23, pp. 8441–8447, 2001.
- [2] A. Chapman and G. Ter Haar, “Thermal ablation of uterine fibroids using mr-guided focused ultrasound-a truly non-invasive treatment modality,” *European radiology*, vol. 17, pp. 2505–2511, 2007.
- [3] K. Hynynen and B. Lulu, “Hyperthermia in cancer treatment,” *Investigative radiology*, vol. 25, no. 7, pp. 824–834, 1990.
- [4] K. Hynynen, “Biophysics and technology of ultrasound hyperthermia,” in *Methods of external hyperthermic heating*. Springer, 1990, pp. 61–115.
- [5] F. A. Duck, A. C. Baker, and H. C. Starritt, *Ultrasound in medicine*. CRC Press, 2020.
- [6] S. B. Raymond, L. H. Treat, J. D. Dewey, N. J. McDannold, K. Hynynen, and B. J. Bacska, “Ultrasound enhanced delivery of molecular imaging and therapeutic agents in alzheimer’s disease mouse models,” *PloS one*, vol. 3, no. 5, p. e2175, 2008.
- [7] B. Billard, K. Hynynen, and R. Roemer, “Effects of physical parameters on high temperature ultrasound hyperthermia,” *Ultrasound in medicine & biology*, vol. 16, no. 4, pp. 409–420, 1990.
- [8] P. Lele, “Production of deep focal lesions by focused ultrasound-current status,” *Ultrasonics*, vol. 5, no. 2, pp. 105–112, 1967.
- [9] J. E. Kennedy, “High-intensity focused ultrasound in the treatment of solid tumours,” *Nature reviews cancer*, vol. 5, no. 4, pp. 321–327, 2005.
- [10] T. J. Dubinsky, C. Cuevas, M. K. Dighe, O. Kolokythas, and J. H. Hwang, “High-intensity focused ultrasound: current potential and oncologic applications,” *American journal of roentgenology*, vol. 190, no. 1, pp. 191–199, 2008.
- [11] H. E. Cline, J. F. Schenck, K. Hynynen, R. D. Watkins, S. P. Souza, and F. A. Jolesz, “Mr-guided focused ultrasound surgery,” *Journal of computer assisted tomography*, vol. 16, no. 6, pp. 956–965, 1992.
- [12] D. Gianfelice, A. Khiat, M. Amara, A. Belblidia, and Y. Boulanger, “Mr imaging-guided focused us ablation of breast cancer: histopathologic assessment of effectiveness—initial experience,” *Radiology*, vol. 227, no. 3, pp. 849–855, 2003.
- [13] E. Martin, D. Jeanmonod, A. Morel, E. Zadicario, and B. Werner, “High-intensity focused ultrasound for noninvasive functional neurosurgery,” *Annals of Neurology: Official Journal of the American Neurological Association and the Child Neurology Society*, vol. 66, no. 6, pp. 858–861, 2009.
- [14] N. McDannold, E.-J. Park, C.-S. Mei, E. Zadicario, and F. Jolesz, “Evaluation of three-dimensional temperature distributions produced by a low-frequency transcranial focused ultrasound system

within ex vivo human skulls,” *IEEE transactions on ultrasonics, ferroelectrics, and frequency control*, vol. 57, no. 9, pp. 1967–1976, 2010.

- [15] M. Lepetit-Coiffé, H. Laumonier, O. Seror, B. Quesson, M.-B. Sesay, C. T. Moonen, N. Grenier, and H. Trillaud, “Real-time monitoring of radiofrequency ablation of liver tumors using thermal-dose calculation by mr temperature imaging: initial results in nine patients, including follow-up,” *European radiology*, vol. 20, pp. 193–201, 2010.
- [16] J. Hindman, “Proton resonance shift of water in the gas and liquid states,” *The Journal of Chemical Physics*, vol. 44, no. 12, pp. 4582–4592, 1966.
- [17] Y. Ishihara, A. Calderon, H. Watanabe, K. Okamoto, Y. Suzuki, K. Kuroda, and Y. Suzuki, “A precise and fast temperature mapping using water proton chemical shift,” *Magnetic resonance in medicine*, vol. 34, no. 6, pp. 814–823, 1995.
- [18] K. Kuroda, “Non-invasive mr thermography using the water proton chemical shift,” *International journal of hyperthermia*, vol. 21, no. 6, pp. 547–560, 2005.
- [19] N. Bloembergen, E. M. Purcell, and R. V. Pound, “Relaxation effects in nuclear magnetic resonance absorption,” *Physical review*, vol. 73, no. 7, p. 679, 1948.
- [20] D. L. Parker, “Applications of nmr imaging in hyperthermia: an evaluation of the potential for localized tissue heating and noninvasive temperature monitoring,” *IEEE transactions on biomedical engineering*, no. 1, pp. 161–167, 1984.
- [21] T. Nelson and S. Tung, “Temperature dependence of proton relaxation times in vitro,” *Magnetic resonance imaging*, vol. 5, no. 3, pp. 189–199, 1987.
- [22] V. Rieke and K. Butts Pauly, “Mr thermometry,” *Journal of Magnetic Resonance Imaging: An Official Journal of the International Society for Magnetic Resonance in Medicine*, vol. 27, no. 2, pp. 376–390, 2008.
- [23] A. Abragam, *The principles of nuclear magnetism*. Oxford university press, 1961, no. 32.
- [24] F. H. Johnson, H. Eyring, and B. J. Stover, “The theory of rate processes in biology and medicine,” (*No Title*), 1974.
- [25] J. Chen, B. L. Daniel, and K. B. Pauly, “Investigation of proton density for measuring tissue temperature,” *Journal of Magnetic Resonance Imaging: An Official Journal of the International Society for Magnetic Resonance in Medicine*, vol. 23, no. 3, pp. 430–434, 2006.
- [26] A. Sai, T. Shimono, K. Sakai, A. Takeda, H. Shimada, T. Tsukamoto, H. Maeda, S. Sakamoto, and Y. Miki, “Diffusion-weighted imaging thermometry in multiple sclerosis,” *Journal of Magnetic Resonance Imaging*, vol. 40, no. 3, pp. 649–654, 2014.
- [27] H. E. Cline, K. Hynynen, E. Schneider, C. J. Hardy, S. E. Maier, R. D. Watkins, and F. A. Jolesz, “Simultaneous magnetic resonance phase and magnitude temperature maps in muscle,” *Magnetic resonance in medicine*, vol. 35, no. 3, pp. 309–315, 1996.
- [28] G. Stockman and L. G. Shapiro, *Computer vision*. Prentice Hall PTR, 2001.

- [29] M. Wang, S. Zheng, X. Li, and X. Qin, “A new image denoising method based on gaussian filter,” in *2014 International Conference on information science, electronics and electrical engineering*, vol. 1. IEEE, 2014, pp. 163–167.
- [30] C. Tomasi and R. Manduchi, “Bilateral filtering for gray and color images,” in *Sixth international conference on computer vision (IEEE Cat. No. 98CH36271)*. IEEE, 1998, pp. 839–846.
- [31] M. Elad, “On the origin of the bilateral filter and ways to improve it,” *IEEE Transactions on image processing*, vol. 11, no. 10, pp. 1141–1151, 2002.
- [32] B. Zhang and J. P. Allebach, “Adaptive bilateral filter for sharpness enhancement and noise removal,” *IEEE transactions on Image Processing*, vol. 17, no. 5, pp. 664–678, 2008.
- [33] A. Buades, B. Coll, and J.-M. Morel, “A non-local algorithm for image denoising,” in *2005 IEEE computer society conference on computer vision and pattern recognition (CVPR ’05)*, vol. 2. IEEE, 2005, pp. 60–65.
- [34] X. Zhang, G. Hou, J. Ma, W. Yang, B. Lin, Y. Xu, W. Chen, and Y. Feng, “Denoising mr images using non-local means filter with combined patch and pixel similarity,” *PloS one*, vol. 9, no. 6, p. e100240, 2014.
- [35] K. Song, Q. Ling, Z. Li, and F. Li, “An improved mri denoising algorithm based on wavelet shrinkage,” in *The 26th Chinese Control and Decision Conference (2014 CCDC)*. IEEE, 2014, pp. 2995–2999.
- [36] P. Anandan, A. Giridhar, E. I. Lakshmi, and P. Nishitha, “Medical image denoising using fast discrete curvelet transform,” *Int. J.*, vol. 8, pp. 3760–3765, 2020.
- [37] L. I. Rudin, S. Osher, and E. Fatemi, “Nonlinear total variation based noise removal algorithms,” *Physica D: nonlinear phenomena*, vol. 60, no. 1-4, pp. 259–268, 1992.
- [38] A. Chambolle, “An algorithm for total variation minimization and applications,” *Journal of Mathematical imaging and vision*, vol. 20, pp. 89–97, 2004.
- [39] K. Bredies, K. Kunisch, and T. Pock, “Total generalized variation,” *SIAM Journal on Imaging Sciences*, vol. 3, no. 3, pp. 492–526, 2010.
- [40] M. Elad and M. Aharon, “Image denoising via sparse and redundant representations over learned dictionaries,” *IEEE Transactions on Image processing*, vol. 15, no. 12, pp. 3736–3745, 2006.
- [41] F. Baselice, G. Ferraioli, V. Pascazio, and A. Sorriso, “Bayesian mri denoising in complex domain,” *Magnetic resonance imaging*, vol. 38, pp. 112–122, 2017.
- [42] Z. Xu and Q. Shi, “Denoising model for parallel magnetic resonance imaging images using higher-order markov random fields,” *IET Image Processing*, vol. 10, no. 12, pp. 962–970, 2016.
- [43] A. Krizhevsky, I. Sutskever, and G. E. Hinton, “Imagenet classification with deep convolutional neural networks,” *Advances in neural information processing systems*, vol. 25, 2012.
- [44] I. Goodfellow, J. Pouget-Abadie, M. Mirza, B. Xu, D. Warde-Farley, S. Ozair, A. Courville, and Y. Bengio, “Generative adversarial nets,” *Advances in neural information processing systems*, vol. 27, 2014.

- [45] K. Zhang, W. Zuo, Y. Chen, D. Meng, and L. Zhang, “Beyond a gaussian denoiser: Residual learning of deep cnn for image denoising,” *IEEE transactions on image processing*, vol. 26, no. 7, pp. 3142–3155, 2017.
- [46] W. Wang, “An improved denoising model for convolutional neural network,” in *Journal of Physics: Conference Series*, vol. 1982, no. 1. IOP Publishing, 2021, p. 012169.
- [47] O. Ronneberger, P. Fischer, and T. Brox, “U-net: Convolutional networks for biomedical image segmentation,” in *Medical image computing and computer-assisted intervention—MICCAI 2015: 18th international conference, Munich, Germany, October 5-9, 2015, proceedings, part III 18*. Springer, 2015, pp. 234–241.
- [48] J. Gurrola-Ramos, O. Dalmau, and T. E. Alarcón, “A residual dense u-net neural network for image denoising,” *IEEE Access*, vol. 9, pp. 31 742–31 754, 2021.
- [49] H. Zhang, Q. Lian, J. Zhao, Y. Wang, Y. Yang, and S. Feng, “Ratunet: residual u-net based on attention mechanism for image denoising,” *PeerJ Computer Science*, vol. 8, p. e970, 2022.
- [50] F. Vega, A. Addeh, and M. E. MacDonald, “Denoising simulated low-field mri (70mt) using denoising autoencoders (dae) and cycle-consistent generative adversarial networks (cycle-gan),” *arXiv preprint arXiv:2307.06338*, 2023.
- [51] M. Arjovsky and L. Bottou, “Towards principled methods for training generative adversarial networks,” *arXiv preprint arXiv:1701.04862*, 2017.
- [52] M. Arjovsky, S. Chintala, and L. Bottou, “Wasserstein generative adversarial networks,” in *International conference on machine learning*. PMLR, 2017, pp. 214–223.
- [53] I. Gulrajani, F. Ahmed, M. Arjovsky, V. Dumoulin, and A. C. Courville, “Improved training of wasserstein gans,” *Advances in neural information processing systems*, vol. 30, 2017.
- [54] M. Ran, J. Hu, Y. Chen, H. Chen, H. Sun, J. Zhou, and Y. Zhang, “Denoising of 3d magnetic resonance images using a residual encoder–decoder wasserstein generative adversarial network,” *Medical image analysis*, vol. 55, pp. 165–180, 2019.
- [55] R. J. Hyndman, “Moving averages.” 2011.
- [56] A. Savitzky and M. J. Golay, “Smoothing and differentiation of data by simplified least squares procedures.” *Analytical chemistry*, vol. 36, no. 8, pp. 1627–1639, 1964.
- [57] J. Law, “Robust statistics—the approach based on influence functions,” 1986.
- [58] J. Fan, *Local polynomial modelling and its applications: monographs on statistics and applied probability 66*. Routledge, 2018.
- [59] M. Avery, “Literature review for local polynomial regression,” *Unpublished manuscript*, 2013.
- [60] W. S. Cleveland and S. J. Devlin, “Locally weighted regression: an approach to regression analysis by local fitting,” *Journal of the American statistical association*, vol. 83, no. 403, pp. 596–610, 1988.
- [61] C. De Boor, “A practical guide to splines,” *Springer-Verlag google schola*, vol. 2, pp. 4135–4195, 1978.

- [62] E. Bertolazzi, M. Frego, and F. Biral, “Point data reconstruction and smoothing using cubic splines and clusterization,” *Mathematics and Computers in Simulation*, vol. 176, pp. 36–56, 2020.
- [63] I. Azizan, S. A. B. A. Karim, and S. S. K. Raju, “Fitting rainfall data by using cubic spline interpolation,” in *MATEC Web of Conferences*, vol. 225. EDP Sciences, 2018, p. 05001.
- [64] G. Farin, *Curves and surfaces for computer-aided geometric design: a practical guide*. Elsevier, 2014.
- [65] W. A. F. W. Amir, M. Y. Misro, and M. H. Mohd, “Flexible functional data smoothing and optimization using beta spline,” *AIMS Mathematics*, vol. 9, no. 9, pp. 23 158–23 181, 2024.
- [66] S. G. Mallat, “A theory for multiresolution signal decomposition: the wavelet representation,” *IEEE transactions on pattern analysis and machine intelligence*, vol. 11, no. 7, pp. 674–693, 1989.
- [67] G. Strang and T. Nguyen, “Wavelets and filter banks, wellesley-cambridge press,” *Hardcover, UK,(October 1996)*, 1996.
- [68] X. Dai, L. Z. Cheng, J.-C. Mareschal, D. Lemire, and C. Liu, “New method for denoising borehole transient electromagnetic data with discrete wavelet transform,” *Journal of Applied Geophysics*, vol. 168, pp. 41–48, 2019.
- [69] A. Filippou, N. Evripidou, and C. Damianou, “Robotic system for magnetic resonance imaging-guided focused ultrasound treatment of thyroid nodules,” *The International Journal of Medical Robotics and Computer Assisted Surgery*, vol. 19, no. 5, p. e2525, 2023.
- [70] T. Drakos, M. Giannakou, G. Menikou, and C. Damianou, “Magnetic resonance imaging-guided focused ultrasound positioning system for preclinical studies in small animals,” *Journal of Ultrasound in Medicine*, vol. 40, no. 7, pp. 1343–1352, 2021.
- [71] C. Rother, V. Kolmogorov, and A. Blake, ““grabcut” interactive foreground extraction using iterated graph cuts,” *ACM transactions on graphics (TOG)*, vol. 23, no. 3, pp. 309–314, 2004.
- [72] Y. Boykov and V. Kolmogorov, “An experimental comparison of min-cut/max-flow algorithms for energy minimization in vision,” *IEEE transactions on pattern analysis and machine intelligence*, vol. 26, no. 9, pp. 1124–1137, 2004.
- [73] M. Juneja, A. Rathee, R. Verma, R. Bhutani, S. Baghel, S. K. Saini, and P. Jindal, “Denoising of magnetic resonance images of brain tumor using bt-autonet,” *Biomedical Signal Processing and Control*, vol. 87, p. 105477, 2024.
- [74] Z. Wang, A. C. Bovik, H. R. Sheikh, and E. P. Simoncelli, “Image quality assessment: from error visibility to structural similarity,” *IEEE Transactions on Image Processing*, vol. 13, no. 4, pp. 600–612, 2004.
- [75] A. Antoniou, M. Giannakou, N. Evripidou, S. Stratis, S. Pichardo, and C. Damianou, “Robotic system for top to bottom mrgfus therapy of multiple cancer types,” *The International Journal of Medical Robotics and Computer Assisted Surgery*, vol. 18, no. 2, p. e2364, 2022.